

***Final Draft***  
**of the original manuscript:**

Junior, W.S.; Emmler, T.; Abetz, C.; Handge, U.A.; dos Santos, J.F.;  
Amancio-Filho, S.T.; Abetz, V.:

**Friction spot welding of PMMA with PMMA/silica and  
PMMA/silica-g-PMMA nanocomposites functionalized via ATRP**

In: *Polymer* (2014) Elsevier

DOI: [10.1016/j.polymer.2014.08.022](https://doi.org/10.1016/j.polymer.2014.08.022)

## **Friction Spot Welding of PMMA with PMMA/Silica and PMMA/Silica-g-PMMA Nanocomposites Functionalized via ATRP**

Wiebke S. Junior, Thomas Emmmler, Clarissa Abetz, Ulrich A. Handge, Jorge F. dos Santos, Sergio T. Amancio-Filho\*, Volker Abetz\*

---

\* Corresponding author.

W. S. Junior, Dr. T. Emmmler, C. Abetz, Dr. U. A. Handge  
Helmholtz-Zentrum Geesthacht, Institute of Polymer Research  
Max-Planck-Strasse 1, 21502 Geesthacht, Germany

Dr. J. F. dos Santos  
Helmholtz-Zentrum Geesthacht GmbH, Institute of Materials Research  
Max-Planck-Strasse 1, 21502 Geesthacht, Germany

Prof. S.T. Amancio-Filho  
Helmholtz-Zentrum Geesthacht GmbH, Institute of Materials Research  
Max-Planck-Strasse 1, 21502 Geesthacht, Germany  
E-mail: sergio.amancio@hzg.de  
Phone: +49-4152-87-2066

and

Hamburg University of Technology (TUHH), Institute of Polymer Composites (M11)  
Denickestrasse 15, 21073 Hamburg, Germany

Prof. V. Abetz  
Helmholtz-Zentrum Geesthacht, Institute of Polymer Research  
Max-Planck-Strasse 1, 21502 Geesthacht, Germany  
E-mail: volker.abetz@hzg.de  
Phone: +49-4152-87-2461

and

University of Hamburg, Institute of Physical Chemistry  
Grindelallee 117, 20146 Hamburg, Germany

## Abstract

In the present study, the feasibility of Friction Spot Welding (FSpW) of a commercial-grade poly(methyl methacrylate) (PMMA) (PMMA GS) and PMMA 6N/functionalized silica nanocomposites was investigated. The silica nanoparticles were functionalized via atom transfer radical polymerization (ATRP) with PMMA chains to achieve a uniform dispersion in the polymer matrix. The successful functionalization of silica nanoparticles with PMMA chains via ATRP was evaluated by ATR-FT-IR and TGA measurements. Rheological investigations of the silica nanocomposites showed a plateau of the storage modulus  $G'$  at low frequencies (0.01 to 0.03 rad/s) as a result of elastic particle-particle interactions. Overlap friction spot welds consisting of PMMA GS and a 2 wt% SiO<sub>2</sub>-g-PMMA nanocomposite were successfully prepared and compared to spot joints of PMMA GS welded with PMMA 6N and PMMA 6N/silica nanocomposite with 2 wt% unfunctionalized silica nanoparticles. Raman mappings of selected areas of cross-sectional plastographic specimens revealed an increased mixing behavior between the two polymer plates in the case of PMMA GS/2wt% SiO<sub>2</sub>-g-PMMA joints. Although the joints welded with PMMA 6N/silica nanocomposites showed a reduction of 22% in lap shear strength and 21% displacement at peak load compared with the neat PMMA spot welds, they can compete with other state-of-the-art PMMA welding techniques such as thermal bonding and ultrasonic welding, which indicates the potential of friction spot welding as an alternative fabrication technology for joining future nanocomposite engineering parts.

Keywords: ATRP; silica; PMMA; nanocomposites; Raman spectroscopy; Friction Spot Welding

## 1. Introduction

Today, the development of new, lightweight material solutions plays a central role in the automotive and aerospace industry. Decreases in vehicle weight imply less fuel consumption and thus a reduction of CO<sub>2</sub> emissions, contributing to the preservation of scarce raw material resources. Moreover, the increasing automotive market needs for high comfort, improved safety as well as improved engine efficiencies requires tailor-made materials and cost-effective and innovative manufacturing technologies.

Based on their extraordinarily high surface-to-volume ratio, nanoparticles offer great opportunities to improve the performance of polymers. In 1991, Toyota Motors Co. [1] first commercialized a polyamide/nanoclay composite for the engine cover of cars. Since then, several investigations on nanocomposites for automotive applications have been reported. However, the introduction of nanocomposites into automobiles has been delayed due to technical issues related to their intrinsic properties.

The main challenge is to improve the dispersion of nanoparticles in a matrix and thus utilize their entire range of excellent properties. Inorganic nanofillers in particular tend to agglomerate in an organic polymer matrix. To avoid nanoparticle agglomeration, several approaches to the functionalization of nanoparticles have been investigated. One approach first described by Sawamoto [2] and Matyjaszewski [3] in 1995 is based on atom transfer radical polymerization (ATRP). This technique involves the “*grafting from*” polymerization of polymer chains on nanoparticles with maintenance of a good controlled molecular weight and a rather low polydispersity. Thus, nanocomposites with an enhanced dispersion of nanoparticles in the polymer matrix and improved properties can be achieved. Haase et al. [4] reported an increase of wear resistance up to 85% in the case of PMMA nanocomposites based on silica nanoparticles functionalized via ATRP. Significant improvements in impact resistance for PMMA-reinforced silica nanoparticles functionalized in a double-shell structure were demonstrated by Chakkalakal et al. [5].

The processing of new materials is also an important matter of concern in lightweight structural design. For instance, material connections without filler material or additional reinforced elements or complex geometries present an approach to reducing weight. The Friction Spot Welding (FSpW) process is a friction-based joining technique developed and patented by Helmholtz-Zentrum Geesthacht [6] that offers the possibility of joining similar and dissimilar materials. The Friction Spot Joining (FSpJ) process is a variant recently

introduced in 2012 [7] that enables the joining of composites to metals as well. Good surface quality can be achieved within short joining cycles, which makes FSpW/FSpJ interesting for lightweight applications in the automotive and aerospace industry.

Over the past several years, different studies have been carried out on the FSpJ of polymer/metal hybrid structures, such as aluminum and carbon fiber-reinforced poly(phenylene sulfide) (PPS) [8] or magnesium and carbon fiber/glass fiber-reinforced PPS [9]. The feasibility of the FSpW of thermoplastics was first reported by Oliveira et al. [10] in 2010. The authors investigated the feasibility of friction spot welding overlap joints on 3-mm casting unreinforced PMMA plates. Compared to other welding techniques such as microwave and ultrasonic welding, PMMA spot welding offered an increase in shear strength (9.5 MPa).

This work focuses on the feasibility of welding joints via the FSpW process utilizing tailored PMMA/2wt%-g-PMMA SiO<sub>2</sub> nanocomposites and a commercial-grade PMMA GS.

Nanocomposites consisting of PMMA 6N and Ludox HS 40 silica nanoparticles were prepared. Functionalization of silica nanoparticles with PMMA chains via ATRP was adopted to avoid agglomeration and to achieve a better dispersion in the matrix polymer.

Nanocomposites of PMMA 6N containing 2 wt% functionalized or 2 wt% pristine silica were prepared by solution mixing and subsequent extrusion. The different nanocomposite materials were joined by FSpW with plates of a high-molecular-weight PMMA GS.

In the present work, selected results on the effect of the silica nanoparticles and their functionalization on the joint microstructure of a friction spot weld were investigated. The mechanical performance of single overlap joints was determined by lap shear testing and compared to that offered by other state-of-the-art techniques. Therefore, the outstanding features of both, nanocomposite and the FSpW process, were systematically investigated. It is expected that the FSpW of complex nanocomposite structures will enable new automotive applications in the future such as the direct welding of a wear-resistant nanocomposite headlamp lens on an unreinforced polymer headlamp housing.

## 2. Experimental Approach

### 2.1. Materials

Commercial poly(methyl methacrylate) (PMMA) in granular form (Plexiglas® 6N, Evonik Röhm GmbH, Germany) was used as a matrix material for the preparation of nanocomposites. The number average molar mass was equal to  $M_n = 50$  kg/mol, the weight average molar mass  $M_w = 89$  kg/mol and the polydispersity  $PDI = 1.8$  as revealed by gel permeation chromatography (GPC). The glass transition temperature ( $T_g = 99$  °C) was determined by analysis of the second heating interval of differential scanning calorimetry (DSC) measurements at a rate of 20 K/min. Casted PMMA plates (Plexiglas® PMMA GS, Evonik Röhm GmbH, Germany) with a thickness of 2 mm were machined into specimens measuring 25.4 mm width and 100 mm length. This PMMA grade exhibits a glass transition temperature of 107 °C and a molecular weight of  $M_w = 3065$  kg/mol. The physical properties of PMMA 6N and PMMA GS are listed in Table 1. PMMA GS was selected to simulate the unreinforced material of a headlamp housing, whereas PMMA 6N and its nanocomposites were selected to simulate the headlamp lens.

Nanosilica (Ludox HS-40, 40 wt% colloidal suspension in H<sub>2</sub>O, Sigma-Aldrich Chemie GmbH, Germany), with an average diameter of approx. 12 nm, a surface area of approximately 220 m<sup>2</sup>/g and a density of 1.3 g/cm<sup>3</sup> at 25 °C, was used as received. The following chemicals (Sigma-Aldrich Chemie GmbH, Germany) were obtained and used as received for ATRP reactions: (3-glycidyoxypropyl) trimethoxysilane (GPS) (> 98 %); 2-bromoisobutyryl bromide (2-BriB, 98 %); triethylamine (TEA, ≥ 99 %); N,N,N',N'',N''-pentamethyldiethylenetriamine (PMDETA); copper(I) bromide (Cu(I)Br, 99.99 %, stored under vacuum); anisole (99.7 %); hydrofluoric acid (HF, 48 wt%); and methyl methacrylate (MMA, 99 %), which was purified with an alumina column before use. Tetrahydrofuran (THF) was purchased from Merck KGaA, Germany, and technical-grade methanol (99 %) was obtained from Reher Ramsden GmbH & Co. KG, Germany.

**Table 1: Physical properties of PMMA 6N and PMMA GS**

<b>Polymer</b>	<b>Tensile modulus [MPa]</b>	<b>Tensile Strength [MPa]</b>	<b><math>M_n</math><sup>a)</sup> [kg/mol]</b>	<b><math>M_w</math><sup>a)</sup> [kg/mol]</b>	<b>PDI<sup>a)</sup></b>
PMMA 6N	3200 <sup>b)</sup>	67 <sup>b)</sup>	50	89	1.8
PMMA GS	3300 <sup>c)</sup>	80 <sup>c)</sup>	1505	3065	2.0

<sup>a)</sup> Determined by GPC with RI detector and calibrated to PMMA

<sup>b)</sup> Determined by tensile test

<sup>c)</sup> Data sheet of the manufacturer (Evonik)<sup>[11]</sup>

## 2.2 Analytical methods

Thermogravimetric analysis (TGA) was carried out using a TG 209F1 Iris (NETZSCH Gerätebau GmbH, Germany) to study the grafting performance of the PMMA chains on the silica nanoparticles. The measurements were performed under a constant nitrogen flow of 20 ml/min over a temperature interval of 25 °C to 900 °C at a heating rate of 20 K/min.

Gel permeation chromatography (GPC) was conducted to investigate the number average molar mass ( $M_n$ ), weight average molar mass ( $M_w$ ) and polydispersity. The GPC experiments were performed using a Waters system with PSS-SDV columns (10/100/1000 Å, 5 μ, plus SDV Precolumn), and PMMA was used as a calibration standard.

Attenuated total reflection Fourier transform infrared spectroscopy (ATR-FT-IR) was carried out on an ALPHA FT-IR spectrometer (Bruker Optik GmbH, Germany) to evaluate the successful functionalization of silica nanoparticles after every reaction step. The experiments were performed over a spectral range of 4000 to 375 cm<sup>-1</sup> with 32 scans and a resolution of 4 cm<sup>-1</sup> using an ATR diamond cell at room temperature.

The morphological properties of the nanocomposites were investigated by transmission electron microscopy (TEM) with a FEI Tecnai G<sup>2</sup> F20 (Germany) operated at an electron acceleration voltage of 200 kV in the bright-field mode. Ultrathin sections of cast nanocomposite films and extruded pellets were primed without staining using a Leica Ultracut UCT microtome. Slices measuring approximately 50 nm in thickness were trimmed with a diamond knife.

Rheological measurements were carried out with a rotational rheometer MCR 502 by Anton Paar GmbH (Germany) at 190 °C under a nitrogen atmosphere. A plate-plate geometry with a gap of 1.95 mm was used for the measurements. The cylindrical specimens used for rheological studies were prepared by injection molding. The diameter of the samples was 24 mm and the thickness 2 mm. The samples were conditioned for at least 48 h at 50 °C under vacuum. A melting time of 7 min was employed. To determine the linear viscoelastic range, an amplitude sweep over the range of 1.0 – 10.0 % at an angular frequency of 10 rad/s was performed first. Frequency experiments were then carried out, with the angular frequency set from 100 to 0.01 rad/s with a constant amplitude at  $\gamma_0 = 5\%$  to measure the complex modulus  $G^*$  ( $G^* = G' + i G''$ ).

Cross-sectional specimens cut from the spot weld center were produced according to standard plastographic procedures [12] for optical light microscopy investigations. A Leica DMIRM optical light microscope was used with a 1.6-fold objective in the reflection mode.

A Bruker Senterra Raman Microscope (Bruker Optik GmbH, Germany) with a 785-nm red laser source and a 50-fold objective was used for spectroscopic Raman mappings to determine the material flow and the mixing behavior of the polymers in the spot weld. Measurements were performed using materialographic specimens. The laser power was set to 50 mW, and an aperture of 25  $\mu\text{m}$  was used for all measurements. The mappings consisted of an array of approximately 50 x 40 points with a spacing of approximately 2.4  $\mu\text{m}$  in the x- and y-directions of the plane perpendicular to the incident laser beam. Subsequently, integration of the mapping data was performed for a peak range of 270  $\text{cm}^{-1}$  to 325  $\text{cm}^{-1}$ . This peak range was chosen because it showed the largest change in intensity.

Base material tensile testing was carried out on a Zwick Roell Z020 (Germany) with a load cell of 20 kN. The specimens were prepared according to ISO standard 527-1BA [13] and stored for at least 16 hours under standard conditions [14] prior to measurement. The measurements were performed at a crosshead speed of 1  $\text{mm min}^{-1}$  at ambient temperature, according to the standard ISO 527 [13].

The shear strength of friction spot welds was investigated by lap shear testing according to ASTM D3163 – 01 [15] using a Zwick 1478 universal testing machine (Germany). The

measurements were performed at room temperature (23 °C) at a traverse speed of 2 mm min<sup>-1</sup>. Three replicates were tested for each material combination. Shear strength was calculated by using a nominal area attained from the outer diameter of the sleeve, a common methodology utilized to estimate strength in cases in which the real joined area cannot be experimentally determined.

### 2.3 Functionalization of silica nanoparticles

The functionalization of silica nanoparticles was carried out in three reaction steps: 1) silanization of nanoparticles (Figure 1b); 2) bromination of silane-functionalized nanoparticles (Figure 1c); and 3) “grafting from” polymerization of PMMA via ATRP (Figure 1d). Figure 1 is described in the following sections and summarizes the complete functionalization procedure adopted in this work.

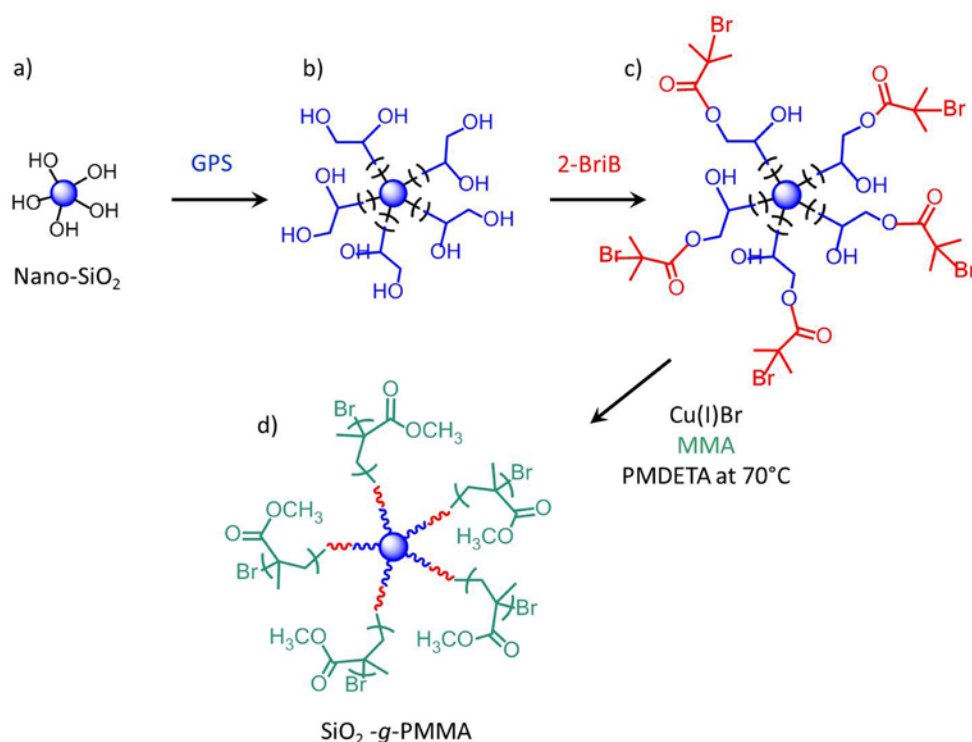


Figure 1: Reaction scheme: a) silica nanoparticles, b) silanization, c) initiator grafting on silica nanoparticles and d) subsequently functionalization with PMMA chains via ATRP

#### 2.3.1 Silanization reaction of silica nanoparticles (Figure 1a - b)

A volume of 100 ml silica Ludox-HS (40 wt% colloidal solution) was placed into a 250-ml round-bottom flask. Subsequently, the silica solution was stirred for at least 30 min on a magnetic stirring plate at a speed of 300 rpm. A volume of 0.32 mol (70 ml) (3-

glycidyloxypropyl) trimethoxysilane was poured into a 100-ml dropping funnel and slowly dropped into the silica solution. To achieve good dispersion, the stirring speed was set to 700 rpm. After the GPS was completely added to the silica, the dispersion was covered with a rubber cap, stirred for a minimum of one hour and set in an ultrasonic bath (Elmasconic S30 H, Elma GmbH & Co KG, Germany) for 3 min. Subsequently, the round-bottom flask was heated to reflux using an oil bath at 85 °C under stirring for 10 min; the temperature was then increased to 90 °C (10 min) and finally to 95 °C to suppress the self-condensation of the silane. The dispersion was stirred for 48 h at 95 °C and then precipitated into 1 l methanol. The precipitated solution was stirred at least for one hour. The silanized silica was then separated from methanol by centrifuging for one hour at 11200 rpm. This cleaning procedure was carried out twice, after which the silanized silica was dissolved in 100 ml toluene.

### 2.3.2 Bromination reaction of silane-functionalized silica nanoparticles (Figure 1c)

After stirring for 12 h in toluene, the silanized silica was transferred into a round-bottom flask; TEA (0.14 mol, 20 ml) was added, and the solution was stirred for 2 h under an argon atmosphere in an ice bath. 2-Bromoisobutyrylbromide (0.06 mol, 7.5 ml) was utilized as a macroinitiator for the ATRP; the initiator was lifted with a syringe and placed in a round-bottom flask while the ice bath was removed and the argon flow stopped. After 48 h, the reaction mixture was precipitated into methanol and centrifuged twice to remove unreacted agents. The brominated silica nanoparticles were dried under vacuum at 50 °C.

### 2.3.3 Modification of silica nanoparticles with PMMA via ATRP (Figure 1d)

Atom transfer radical polymerization (ATRP) was carried out using the brominated silica nanoparticles with molar mass reaction ratios of 200:1:0.8:1 (MMA/initiator/Cu(I)Br/PMDETA and a volume ratio of 1:1 (MMA/anisole). Brominated silica (10.0 g, 5.87 mmol initiator) and anisole (125 ml, 1.15 mol) were placed in a round-bottom flask and stirred for at least 7 h at room temperature (23 °C). The inhibitor was removed by filtering the MMA in a chromatographic column filled with basic aluminum oxide powder. Cu(I)Br (0.674 g, 4.70 mmol) and the MMA (125.0 ml, 1.17 mol) were added to the silica/anisole dispersion. The round-bottom flask was covered with a rubber cap, and the dispersion was stirred for one hour under an argon atmosphere. Subsequently, the round-bottom flask was placed in an oil bath at 70 °C, and PMDETA (1.23 ml, 5.78 mmol) was injected into the dispersion to initialize the ATRP reaction. After 1 h, the reaction was stopped

and the reaction mixture precipitated into 1 l methanol. The product was washed twice with THF; the SiO<sub>2</sub>-g-PMMA was separated by centrifugation and dried in a vacuum oven at 60 °C. A small amount of the functionalized silica nanoparticles was treated with hydrofluoric acid to split off the polymer chains and analyze the molecular mass of the grafted PMMA chains via GPC.

#### **2.4 Preparation of PMMA/silica nanocomposites**

The polymeric matrix PMMA 6N (200 g) was dissolved in approximately 1.5 l THF while the required mass - with respect to the silica content - of functionalized or unfunctionalized silica nanoparticles was separately dissolved in approximately 200 ml THF and stirred for 24 h. The silica was then treated for 5 min in an ultrasonic bath at a frequency of 37 kHz and a power of 80 W. The dispersion was added to the completely dissolved PMMA solution and stirred again for 24 h. The solutions were cast into polypropylene evaporating dishes. The THF was evaporated for 3 days at room temperature. The resulting nanocomposite films (nominal thickness of 3 mm) were crushed into granular-like pieces and dried for 10 days at 80 °C under vacuum.

Extrusion of the nanocomposites was carried out using a Brabender Minicompounder DSE 12/36 D (Brabender GmbH & Co. KG, Germany). A circular die with a diameter of 2 mm was utilized. The five-zone temperature profile from the feed zone to the die was set to 200 °C/220 °C/220 °C/220 °C/220 °C at a screw speed of 120 rpm. The screw configuration included two kneading blocks at 12D and 26D. A venting was also incorporated at 6D.

Specimens for rheological investigations were prepared by injection molding using a Babyplast 6/10P injection molding machine (piston diameter 12 mm, volume 6.5 cm<sup>3</sup>, injection pressure 1850 bar, clamping force 62 kN) from Christmann Kunststofftechnik GmbH (Germany). The temperature was set to 235 °C at the plasticizing piston and the injection piston and to 210 °C at the injection die. The mold temperature used for the specimens was set to 80 °C.

Lap shear test specimens of PMMA 6N and SiO<sub>2</sub> nanocomposites measuring 2 mm in thickness, 100 mm in length and 25.4 mm in width were prepared using P/O/Weber hydraulic pillar heating and cooling presses. The specimens were compression molded at 220 °C and 40 bar, with subsequent cooling for 20 min at 10 bar.

## 2.5 Joining of PMMA/silica nanocomposites and PMMA GS via FSpW

Joining of the neat PMMA 6N and its 2 wt% SiO<sub>2</sub> nanocomposites with PMMA GS was carried out using a RPS 100 FSpW equipment (Harms & Wende, Germany) by the sleeve plunge technique (Figure 2). A titanium tool (TiAl6V4) consisting of a clamping ring, a sleeve and a pin (with outer diameters of 14.5, 9 and 6 mm, respectively) was employed as shown in Figure 2a.

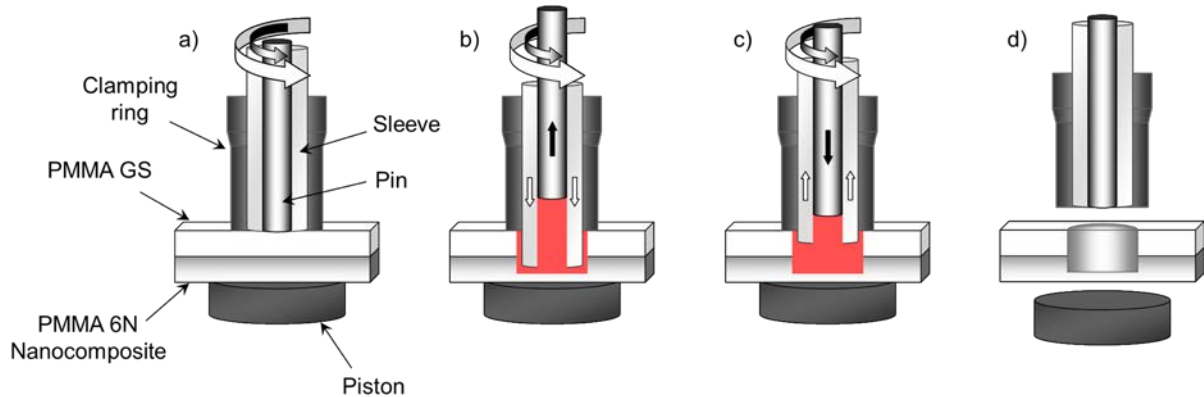


Figure 2: Steps of the Friction Spot Joining process using the sleeve plunge technique: a) polymer plates are clamped between the tool and piston, while the sleeve and pin start to rotate; b) the sleeve penetrates the polymer plates while the pin is retracted and builds a cavity for the softened polymer; c) the pin presses the softened polymer into the joint as the sleeve retracts; d) rotation is stopped, the tool is opened and the joined polymer plates can be removed.

In a previous study, Oliveira et al. [16] reported that titanium tools lead to higher joint strengths compared to those achieved by carbon and stainless steel tools. Due to its low thermal conductivity, titanium maintains the generated frictional heat in the joining area, creating larger welded areas.

Prior to welding, the joining partners (each with dimensions of 2 mm in thickness, 100 mm in length and 25.4 mm in width) are fixed between the clamping ring and the piston (Figure 2a); the PMMA GS plate is then placed onto the PMMA 6N or the SiO<sub>2</sub> nanocomposite plate. The process begins with the plunging of the rotating sleeve into joining partners while the pin is retracted, thus creating a cavity; friction related to the rotation and feeding of the sleeve increases the temperature, softening the PMMA, which flows in the created cavity (Figure 2b). Subsequently, the sleeve is retracted as the pin returns to its starting position, pressing the softened material back into the cavity into the spot welding area, as shown in Figure 2c.

Rotation is stopped as the joint consolidates under pressure to avoid thermal shrinkage. Finally, the clamping is released and the joined specimens are removed (Figure 2d).

The optimized welding conditions were set as follows: a rotational speed of 2000 rpm, a sleeve plunge depth of 2.7 mm and a total welding time of 4.5 s. Table 2 shows the detailed set of welding parameters used in this work.

**Table 2: Friction Spot Welding parameters**

<b>Rotational speed [rpm]</b>	<b>Plunge depth [mm]</b>	<b>Plunge time [s]</b>	<b>Retracting time [s]</b>	<b>Holding pressure time [s]</b>	<b>Holding pressure [bar]</b>
2000	2.7	3	1.5	20	0.8

### 3 Results and Discussion

#### 3.1 Properties of polymer-modified silica nanoparticles

TGA measurements were performed to investigate the efficiency of the individual functionalization steps. The temperature range of interest for the TGA measurements in this study was 100 °C to 750 °C, considering that the mass losses between 750 °C and 900 °C were less than 5 % and therefore not relevant (see Figure 3). To compare the TGA curves of the functionalized nanoparticles with the curve of the pure silica nanoparticles, a sufficient volume of the colloidal silica solution was dried and analyzed as well.

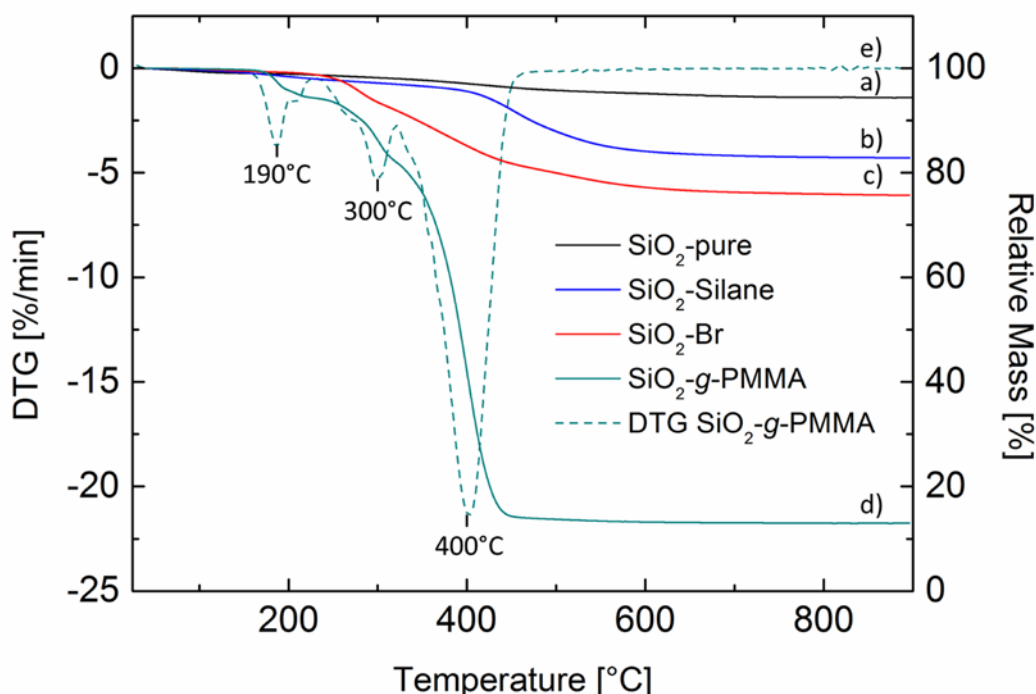


Figure 3: a) Relative mass loss of silica nanoparticles before and after b) silanization, c) bromination and d) “grafting from” polymerization of PMMA. e) Derivative of the thermogravimetric curve of SiO<sub>2</sub>-g-PMMA (heating rate: 20 K/min) as a function of temperature.

Because the weight loss was only approximately 5 wt% over the entire temperature range, the pristine silica nanoparticles (Figure 3a) can be considered to have been thermally stable to a large extent. After silanization of the silica nanoparticles, a mass loss of 14.3 wt% was measured between 100 °C and 750 °C (Figure 3b). The brominated silica nanoparticles

showed a mass loss of 23.1 wt%, which indicates the successful initiator grafting of 0.587 mmol/g on the silica (Figure 3c). According to the ATRP reaction, the TGA curve of PMMA-functionalized silica nanoparticles (Figure 3d) indicates a weight loss of 87 wt% over the temperature range of 100 °C to 750 °C. Considering the fact that the pristine silica showed a weight loss of 5%, a difference in weight loss of 82% could be observed for the PMMA shell on the nanoparticles.

A three-step degradation reaction was additionally observed from the DTG analysis of the PMMA-functionalized nanoparticles (Figure 3e). This phenomenon has been described in several studies as the typical degradation mechanism of PMMA obtained by free radical polymerization, compared to the single-step degradation of PMMA obtained by anionic polymerization [17-21]. Manring et al. [19] investigated the three different degradation steps of radically polymerized PMMA. Based on these results, the first step, with a maximum at approximately 190 °C, can be described as weight loss due to the scission of unsaturated chain ends. The second degradation step, with a maximum at approximately 300 °C, occurs due to weak head-to-head linkages [20], whereas the major degradation step has a maximum at 400 °C, which can be explained by random chain scission along the PMMA macromolecules [21].

GPC measurements were carried out to determine the molar mass of the grafted PMMA chains. To this end, the PMMA chains were degrafted from the silica nanoparticles by hydrofluoric acid treatment. A number average molar mass  $M_n = 36$  kg/mol and a weight average molar mass  $M_w = 43$  kg/mol are achieved with a polydispersity of 1.21. Table 3 summarizes the results of functionalization determined by TGA and GPC.

**Table 3: Functionalization results of silica nanoparticles**

<b>Nanoparticle</b>	<b>Br<sup>a)</sup></b> <b>[mmol/g]</b>	<b>Mass loss<sup>a)</sup></b> <b>[%]</b>	<b>Residual</b> <b>mass<sup>a)</sup></b> <b>[wt%]</b>	<b><math>M_n</math><sup>b)</sup></b> <b>[kg/mol]</b>	<b><math>M_w</math><sup>b)</sup></b> <b>[kg/mol]</b>	<b>PDI<sup>b)</sup></b>
SiO <sub>2</sub> -g-PMMA	0.587	87 <sup>b)</sup>	13	36	43	1.21

<sup>a)</sup> Determined by TGA at a heating rate of 20 °C/min

<sup>b)</sup> Determined by GPC with UV detector calibrated to PMMA

ATR-FT-IR spectroscopy was carried out to confirm the successful grafting of PMMA chains on the silica nanoparticles, as presented in Figure 4. The signal of Si-O-Si stretching at  $1120\text{ cm}^{-1}$  is distinctly shown in the curve of the purified silica Ludox HS 40. After the bromination reaction, the silica nanoparticles showed a C=O stretching peak near  $1730\text{ cm}^{-1}$ , which is caused by the carbonyl group of the macroinitiator. By contrast, the spectrum of SiO<sub>2</sub>-g-PMMA presented additional CH<sub>2</sub> and CH<sub>3</sub> stretching modes in the range of  $2950\text{ cm}^{-1}$  to  $2990\text{ cm}^{-1}$ . These peaks could also be found in the spectra of pure PMMA. This result indicates the successful grafting of PMMA chains on the silica nanoparticles. Furthermore, peaks resulting from bending vibrations of CH<sub>2</sub> at  $1430\text{ cm}^{-1}$  and CH<sub>3</sub> at  $1390\text{ cm}^{-1}$  were detected for SiO<sub>2</sub>-g-PMMA. The intensity of the stretching at  $1730\text{ cm}^{-1}$  increased after ATRP reaction, which can be ascribed to the superposition of the carbonyl groups of the macroinitiator and PMMA.

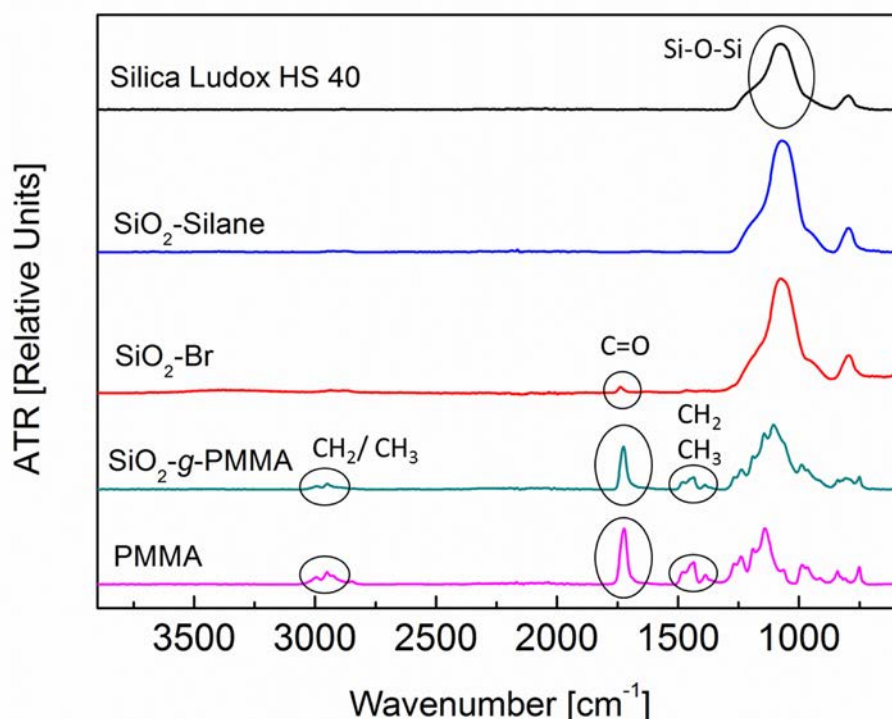


Figure 4: ATR-FT-IR spectra of pristine silica Ludox HS 40, silane-modified silica, brominated silica, SiO<sub>2</sub>-g-PMMA and pristine PMMA.

### 3.2 Morphological properties of PMMA/silica nanocomposites

Morphological investigations were carried out to analyze the efficiency of functionalization on the dispersion of the silica nanoparticles. As shown in Figure 5a, the purified silica formed dense agglomerates with diameters measuring 300 - 500 nm and up to 4  $\mu\text{m}$ . No particles can be observed in the interstices between agglomerates; only a minor number of isolated

nanoparticles are visible at the interface between the agglomerates and the matrix polymer. By contrast, the functionalized silica particles can be observed to have formed agglomerates of nanoparticles with a larger particle-particle distance (Figure 5b).

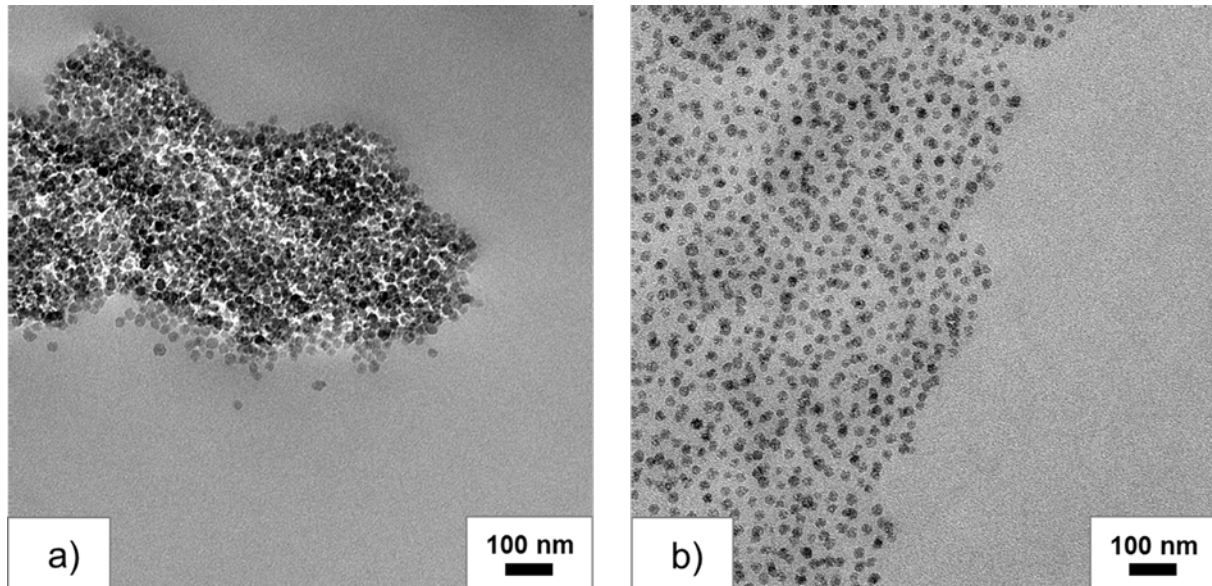


Figure 5: TEM micrograph of a) 2 wt% SiO<sub>2</sub>-pure in PMMA 6N and b) 2 wt% SiO<sub>2</sub>-g-PMMA in PMMA 6N

In contrast to the case of the unfunctionalized nanoparticles, the grafted PMMA chains on the silica nanoparticles led to the separation of the particles. Hence, the functionalized silica nanoparticles did not form dense agglomerates. However, the functionalized nanoparticles still formed larger agglomerates of particles measuring 200 – 400 nm and up to 4  $\mu$ m. To further improve the dispersion of the nanoparticles in the composites, the batches were extruded using a twin screw extruder.

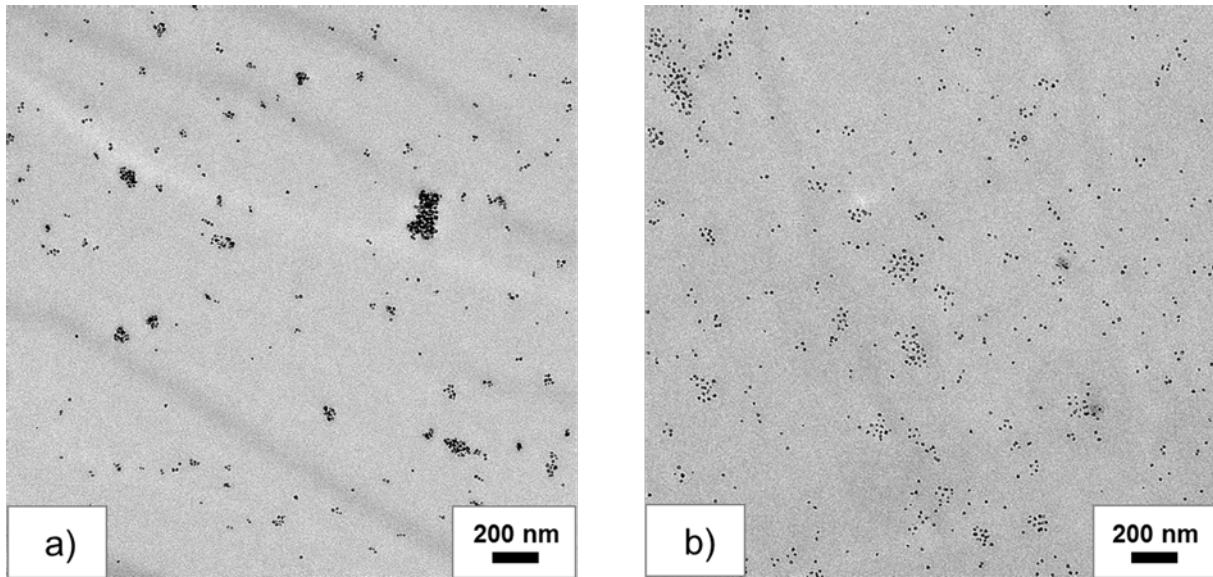


Figure 6: TEM micrograph of a) 2 wt% SiO<sub>2</sub>-pure in PMMA 6N and b) 2 wt% SiO<sub>2</sub>-g-PMMA in PMMA 6N after extrusion

The results of TEM investigations after extrusion are presented in Figure 6. For both composites, better dispersion and the rupture of agglomerates was obtained. In the case of the purified silica (Figure 6a), dense agglomerates with a diameter of approximately 200 nm, but also with diameters of approximately 4 μm, could still be observed. Moreover, smaller agglomerates consisting of 3-10 particles and a minor amount of isolated particles were observed in this composite. The composite composed of 2 wt% SiO<sub>2</sub>-g-PMMA (Figure 6b) still contained some nanoparticle agglomerates in the range of 200 nm to 4 μm. Nevertheless, due to the PMMA chains, the dispersion of the functionalized nanoparticles appears to have improved in the polymer matrix, as indicated by the larger amount of single particles throughout the entire section.

### 3.3 Rheological properties of the pristine polymers and nanocomposites

The results of rheological measurements of pristine PMMA and PMMA/silica nanocomposites are presented in Figure 7. The storage and loss moduli of pristine PMMA 6N show a typical terminal behavior, with  $G' \propto \omega^2$  and  $G'' \propto \omega$ . This behavior indicates a complete relaxation of the PMMA chains. The data obtained for pristine PMMA GS on a double-logarithmic scale show a slight increase in the storage modulus (Figure 7a), whereas the loss modulus curve slightly decreases with increasing angular frequency (Figure 7b). Because of the high molar mass of PMMA GS, the response of the sample is dominated by the entanglement network over the applied range of frequencies, which results in

predominantly elastic behavior (rubbery regime). The effect of incorporating silica nanoparticles is revealed by the plateau of  $G'$  between 0.01 to 0.03 rad/s, which indicates solid-like behavior for both the pristine and functionalized nanoparticles (Figure 7a). This effect is possibly caused by elastic-elastic interactions between neighboring nanoparticles (Figure 7c). A related network effect was also observed by Du et al. [22] for nanocomposites based on 2.5 wt% pristine and 2.5 wt% polystyrene-functionalized carbon nanotubes in a styrene-acrylonitrile copolymer.

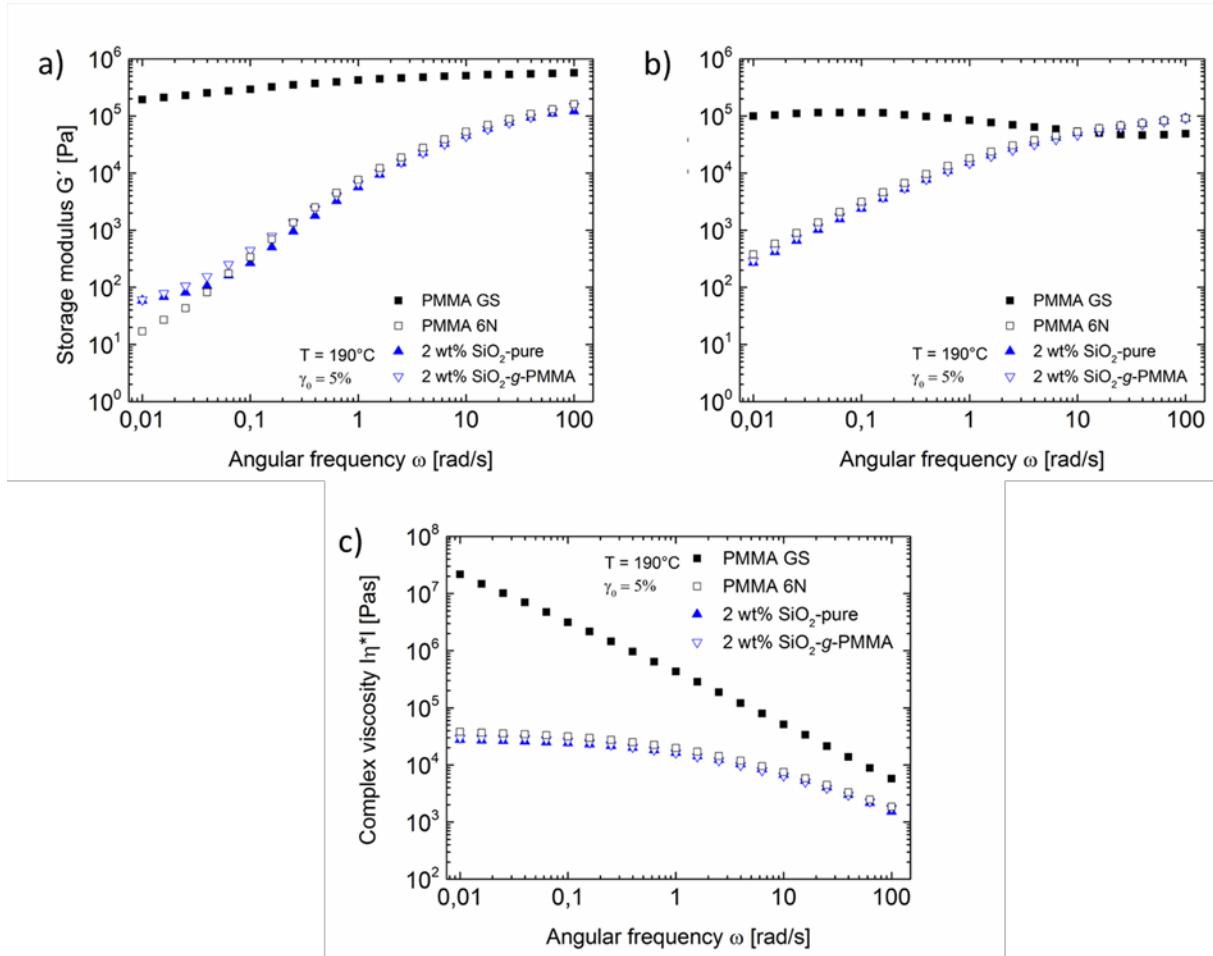


Figure 7: Rheological measurements of a) storage modulus  $G'$ , b) loss modulus  $G''$  and c) magnitude of complex viscosity  $|\eta^*|$  of PMMA GS, PMMA 6N and PMMA/silica nanocomposites as a function of angular frequency at 190 °C.

The complex viscosity decreases for all materials at frequencies above 1 rad/s. At low frequencies, the PMMA GS shows a higher complex viscosity compared to that of the other materials because of the higher molecular weight of this PMMA grade. With increasing frequency, the viscosity of PMMA GS steadily decreases. At an angular frequency of 100 rad/s, only minor differences in viscosity between PMMA GS and the other materials are detected. Because in the FSpW process the joining was performed at a speed of 2000 rpm

(corresponding to a shear rate on the order of 350 1/s), it is assumed that the viscosities of PMMA GS and nanocomposites should not differ greater, as suggested by the extrapolation of the viscosity in Figure 7 c). Thus, the effect of the differences between the viscosities of the materials is less pronounced at large shear rates, and a uniform flow and mix of the softened polymer can be assumed due to the similar viscosities.

Previous rheological investigations of PMMA nanocomposites based on unfunctionalized silica nanoparticles were carried out by Münstedt et al. [23, 24]. PMMA 6N and PMMA 7N were used as matrix materials with a filler content of 2.1 vol% silica with a diameter of 20 nm. The results showed an increase in the storage and loss moduli for nanocomposites compared to those of neat matrix materials. In the current work, only an increase in  $G'$  at low frequencies was detected for the nanocomposites, which can be explained by the smaller diameter of the nanoparticles and a smaller filler content of 2 wt% in the nanocomposites. The reported data indicate that the particle-particle interactions of the nanoparticles in the work of Münstedt et al. [23, 24] led to a more pronounced effect of the nanoparticles on the rheological properties compared to the results presented in this work.

### **3.4 Mechanical properties of the pristine polymer and nanocomposites**

The tensile strengths of pristine PMMA 6N, unfunctionalized 2 wt% SiO<sub>2</sub> in PMMA 6N and functionalized 2 wt% SiO<sub>2</sub>-g-PMMA in PMMA 6N are presented in Figure 8a. For each material, five replicates were tested. It is well known that the interphase between inorganic silica nanoparticles and the organic polymer matrix plays a key role in improving the mechanical properties of the nanocomposites. To benefit from the silica nanoparticles, the applied stress has to be transferred through this interphase to the silica core. The grafted chains on the silica nanoparticles can improve the stress transfer between the silica nanoparticles and the polymer matrix.

Chakkalakal et al. [25] investigated the effect of filler content and silica nanoparticle diameter as well as different molecular weights and different weight fractions of grafted PMMA chains on the mechanical properties of PMMA/SiO<sub>2</sub> nanocomposites. A weight loading of 1.5 wt% SiO<sub>2</sub>-g-PMMA with a diameter of 12 nm, molecular weight of 31 kg/mol and a weight fraction of 58 wt% led to an improvement in the tensile properties compared to the properties observed for the neat PMMA matrix and a nanocomposite of PMMA containing 1.5 wt% unfunctionalized SiO<sub>2</sub>. Furthermore, the authors showed that the tensile properties decreased

with an increasing weight fraction of the PMMA chains on the silica nanoparticles up to 83 wt%. They also reported that the incorporation of 2 wt% silica nanoparticles led to a decrease in tensile properties.

These results confirm the tensile strength data obtained in the present work. The neat PMMA 6N presented an ultimate tensile strength of  $67.2 \pm 4.6$  MPa and demonstrated an ultimate tensile strength level similar to that of the PMMA/2 wt% SiO<sub>2</sub>-pure nanocomposite ( $67.8 \pm 1.9$  MPa), whereas for the PMMA/2 wt% SiO<sub>2</sub>-g-PMMA nanocomposite, a decreased tensile strength of  $57.7 \pm 6.1$  MPa was observed. It is assumed that the high weight fraction of 82 wt% grafted PMMA chains on the silica nanoparticles led to a decrease in the number of entanglements within the polymer matrix. Hence, this material rather than the neat PMMA 6N collapsed.

The change in displacement at the peak load shows similar behavior (Figure 8b). In the figure, PMMA 6N ( $0.82 \pm 0.16$  mm) and the PMMA/2 wt% SiO<sub>2</sub>-pure nanocomposite ( $0.75 \pm 0.12$  mm) exhibit an equal displacement; whereas the PMMA/2 wt% SiO<sub>2</sub>-g-PMMA nanocomposite presents a reduced displacement at a peak load of  $0.48 \pm 0.09$  mm. The increased brittleness of the PMMA/2 wt% SiO<sub>2</sub>-g-PMMA nanocomposite can be explained by the stress concentration caused by the nanoparticles.

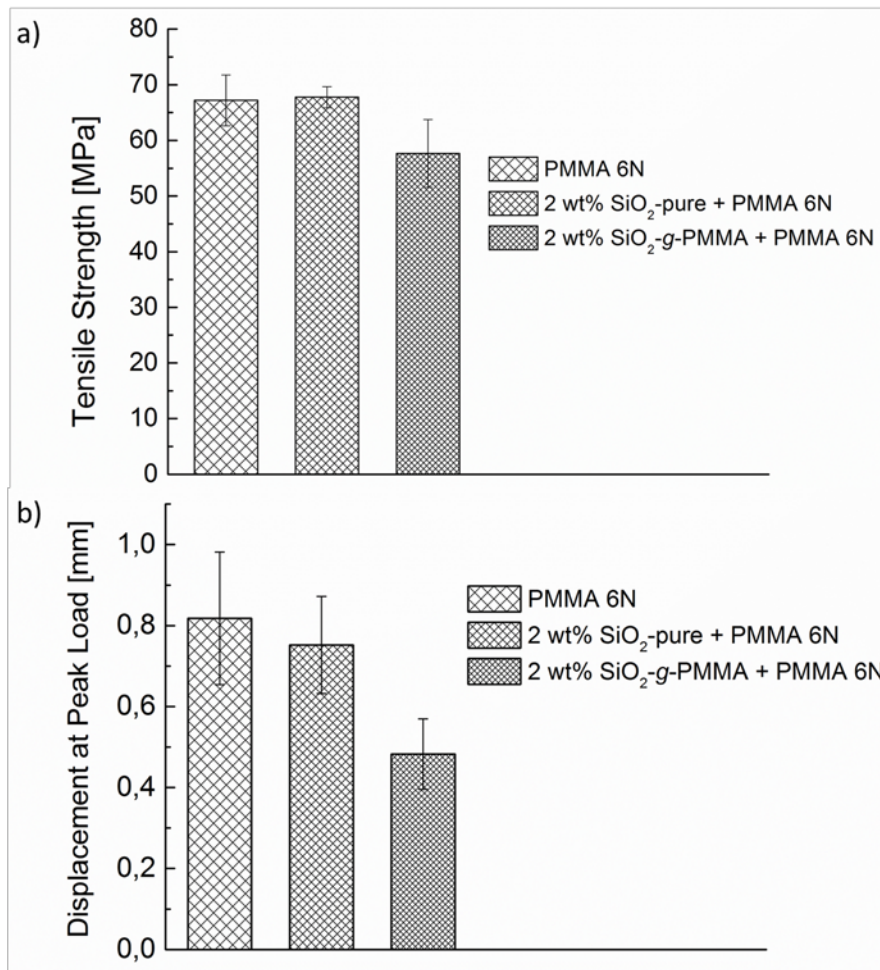


Figure 8: a) Tensile strength and b) displacement at peak load of PMMA 6N, 2 wt% SiO<sub>2</sub>-pure and 2 wt% SiO<sub>2</sub>-g-PMMA in PMMA 6N.

### 3.5 Microstructure of the FSpW joints

Optical light microscopy using reflected light was performed to study the microstructure of the welded spot joints. Figure 9a shows the mid cross-sections of neat PMMA GS welded onto neat PMMA 6N (herein called PMMA GS/PMMA 6N). For comparison purposes, a previously published weld [26] on PMMS GS and PMMA 6N/2 wt% SiO<sub>2</sub>-pure nanocomposite (PMMA GS/2 wt%SiO<sub>2</sub>-pure) is shown in Figure 9b, whereas Figure 9c shows the lap weld of PMMA GS and the PMMA 6N nanocomposite based on 2 wt% SiO<sub>2</sub>-g-PMMA nanoparticles (herein called PMMA GS/2 wt% SiO<sub>2</sub>-g-PMMA). In the micrographs, the upper plate consists of PMMA GS and the lower plate of PMMA 6N or SiO<sub>2</sub> nanocomposites. A friction spot weld on thermoplastics typically shows three characteristic microstructural regions [10]: the stir zone (SZ), the inner heat affected zone and the outer heat affected zone (HAZ) (Figures 10b – d).

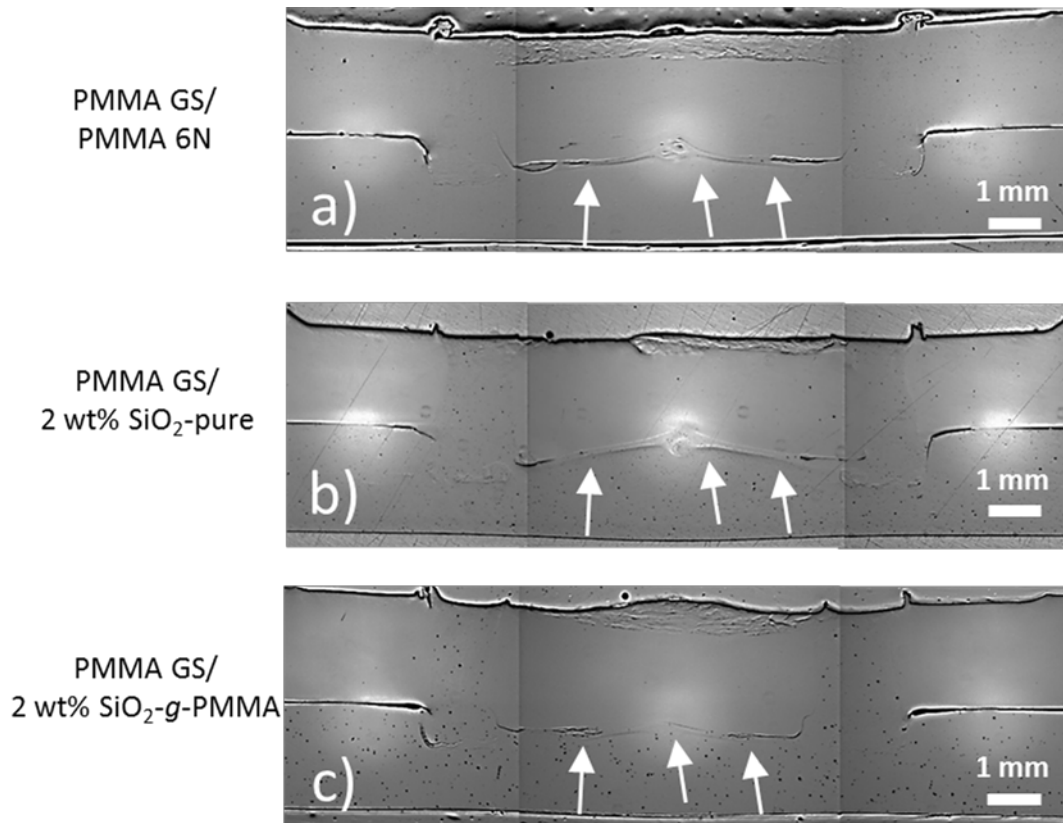


Figure 9: Optical light microscopy images of a) PMMA GS/PMMA 6N, b) PMMA GS/2 wt% SiO<sub>2</sub>-pure and c) PMMA GS/2 wt% SiO<sub>2</sub>-g-PMMA joints

The SZ is the region where the sleeve of the FSpW tool plunges into the polymer plates, softening the base material (process temperatures above  $T_g$  for amorphous and above  $T_m$  for semicrystalline polymers), and the resulting keyhole is refilled by the softened polymer. In the HAZ, temperatures are normally below  $T_g$  (and hence the polymer behaves as a solid) and no visual changes can be detected relative to the base materials. Oliveira et al. [10] showed that a slight decrease in microhardness can be observed in this region, which may indicate the onset of depolymerization reactions in PMMA.

In this study, the rotational speed was set to 2000 rpm for all material combinations. In another study, Junior et al. [26] observed that this rotational speed led to improved heat input, resulting in fewer thermo-mechanical changes in the welded area of PMMA lap joints. The authors analyzed the effects of various rotational speeds on the different weld microstructural zones and showed that with an increasing rotational speed (meaning an increasing in heat input) enhanced softening (decrease of melt viscosity) of the polymer occurs, resulting in an improved refilling of the SZ. In addition, spot welds produced at higher rotational speeds (3000 rpm) resulted in welds with improved softening of the polymer plates compared with joints welded at lower rotational speeds (1000 rpm). In the current work, the incorporation of

silica nanoparticles showed a similar trend with the rotational speed. The addition of silica nanoparticles resulted in better refilling and final microstructures of the nanocomposites than of the neat PMMA. This general trend is probably associated with the increase in thermal conductivity related to the addition of silica nanoparticles [27].

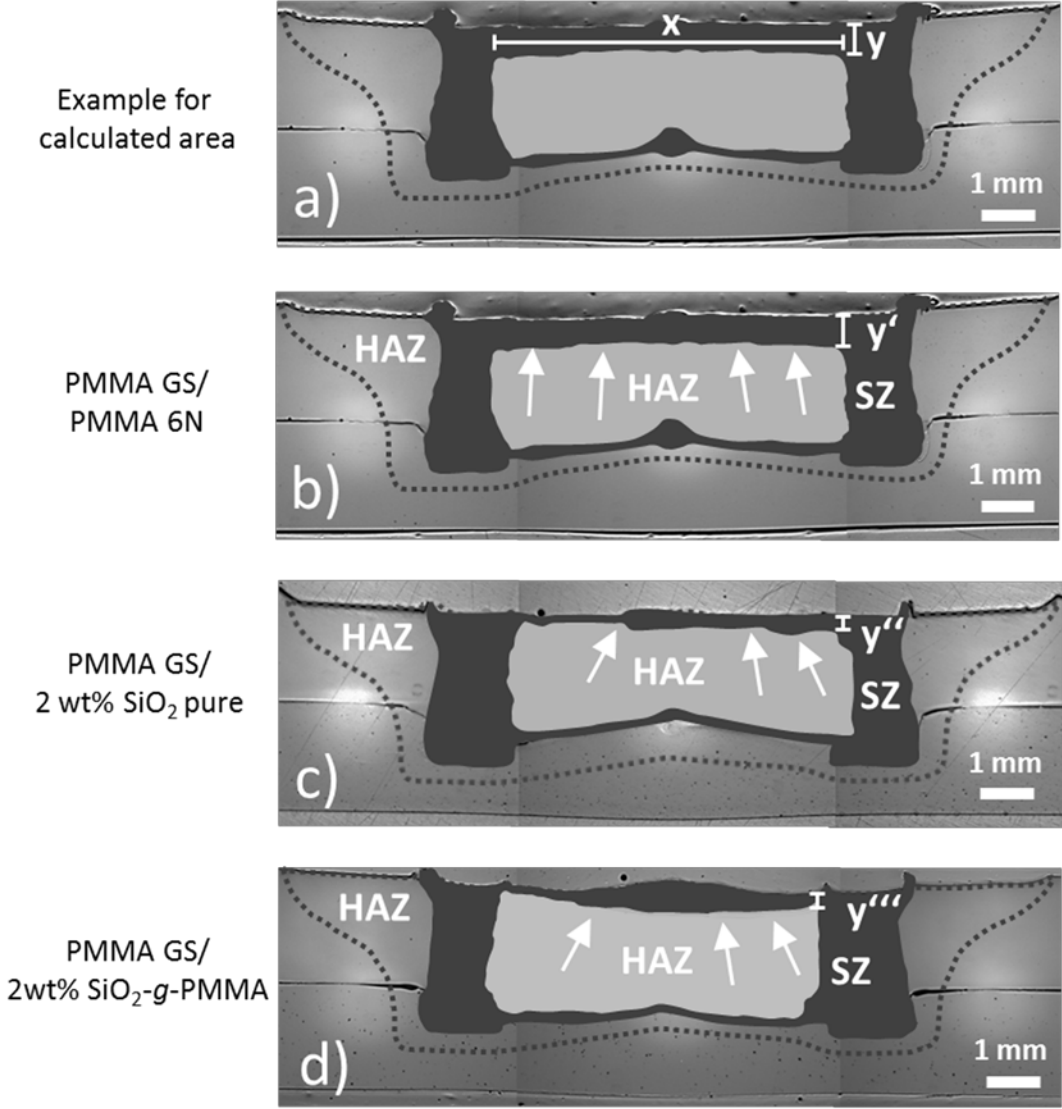


Figure 10: a) Example of calculated area of softened polymer in the upper region of the SZ:  $y$  indicates the average thickness of the softened polymer, whereas  $x$  marks the outer diameter of the pin. Different microstructural zones detected in the FSpW joints: b) PMMA GS/PMMA 6N, c) PMMA GS/2 wt% SiO<sub>2</sub>-pure and d) PMMA GS/2 wt% SiO<sub>2</sub>-g-PMMA. The dark grey area indicates the stir zone (SZ), the light grey area indicates the inner heat affected zone (HAZ) and the dotted line indicates the outer HAZ.

As expected, all welded joints presented a microstructure containing no volumetric defects related to inadequate material flow or extensive thermo-mechanical degradation.

Nevertheless, in the upper region of the SZ in particular, changes in the joint microstructure

could be observed for different welded material combinations. To quantify the volume of softened polymer in this region, a rectangular area, calculated from the average thickness  $y$  (obtained from the graphical measurements of the different microstructural zones; see Figure 10a: example of calculated area, mark:  $y$ ) and the pin's external diameter ( $x = 6$  mm), was considered. Table 4 summarizes the results of all three analyzed material combinations. The PMMA GS/PMMA 6N spot weld presented a larger volume of softened polymer (area  $a' = 3.6$  mm<sup>2</sup>) in the upper region of the SZ, as indicated by arrows in Figure 9d. By contrast, the joints produced with PMMA GS/2 wt% SiO<sub>2</sub>-pure (see Figure 10c,  $y'' = 0.3$  mm) and PMMA GS/2 wt% SiO<sub>2</sub>-g-PMMA (see Figure 10d,  $y''' = 0.3$  mm) both showed an area of approximately 1.8 mm<sup>2</sup>. This value corresponds to a reduction of approximately 50 % in the amount of softened polymer, which indicates the improved refilling of the welded area. Due to the higher heat conductivity of the SiO<sub>2</sub> nanoparticles, the softening (decrease in viscosity) of the polymer was enhanced; the frictional heat generated by the tool shearing was conducted more homogeneously through the polymer matrix, resulting in a larger amount of softened polymer. Therefore, for this joint, more softened material refilled the spot weld and the pin was able to push the increased amount of polymer melt back into the joint.

**Table 4: Results of calculated areas of softened polymer in the upper region of the SZ for all spot welds**

<b>Sample</b>	<b>x (pin's outer diameter) [mm]</b>	<b>y (average polymer thickness) [mm]</b>	<b>a (calculated area) [mm<sup>2</sup>]</b>
PMMA GS/PMMA 6N	6	0.6	3.6
PMMA GS/2 wt% SiO <sub>2</sub> -pure	6	0.3	1.8
PMMA GS/2 wt% SiO <sub>2</sub> -g-PMMA	6	0.3	1.8

The effect of material mixing can be further investigated by analyzing the presence of a weld line at the interface between the upper and lower plates at the spot weld center. For the joint of PMMA GS/PMMA 6N, a more pronounced weld line was observed (Figure 9a, white arrows). In contrast, the joint center of PMMA GS/2 wt%SiO<sub>2</sub>-pure showed a smoother weld line (Figure 9b). The PMMA GS/2 wt% SiO<sub>2</sub>-g-PMMA joint displayed an improved smoothing of the weld line. Lin et al. [28] analyzed the effect of higher heat input on PMMA during the spin friction welding process. The authors identified partially and completely

softened weld zones as well as a central non-softened region (a sharp interface between joining partners). With increasing heat input (e.g., achieved by increasing the welding time), the partially and completely softened regions expanded and the non-softened region disappeared. Because mechanical mixing due to the sleeve is not expected to occur at the center of friction spot welds (inner HAZ), an effect similar to that observed for spin welding joints can be identified. Because the shear rates at the center of the spot weld are lower compared to those in the regions adjacent to the rotating sleeve, no mixing between the polymers is expected to occur in this region.

Wool and O'Connor [29] proposed five main steps that occur during polymer welding: a) rearrangement of the polymer chains, b) approach of two welding surfaces, c) wetting, d) interdiffusion and e) randomization of molecular chains. Considering this five steps, at the center of the spot welds created in this work, it is likely that only wetting between the upper and lower base materials in the PMMA GS/PMMA 6N joint occurred. As mentioned previously, the incorporation of SiO<sub>2</sub> nanoparticles leads to increased polymer softening, due to improved thermal conductivity. Therefore, the joint of PMMA GS/2 wt% SiO<sub>2</sub>-pure showed a less pronounced weld line at the joint center.

The functionalization of SiO<sub>2</sub> nanoparticles with PMMA chains leads to an improved distribution of the particles and consequently a better heat distribution by conduction. In addition, the polymer chains in the silica nanocomposites appear to act like a compatibilizer between the two matrix polymers. Thus, the weld line at the spot weld center of PMMA GS/2% SiO<sub>2</sub>-g-PMMA was smoother than the weld lines of the welds formed with unfunctionalized silica particles.

### **3.6 Material flow and mixing in the FSpW joints**

Raman spectra were generated to investigate the material flow and the mixing behavior of the polymers in the spot welds. The material flow (white arrows) and mixing of friction spot welds between neat and nanocomposite PMMA are schematically illustrated in Figure 11. When the sleeve reaches the lower nanocomposite plate, heat softens the polymer, leading to a decrease in viscosity; therefore, nanoparticles are transferred to the flowing material, redistributed by the stirring action of the sleeve and mixed with the softened polymer matrix within the SZ. In the regions adjacent to the rotating sleeve, the shear rates are greater than

those at the center of the spot weld. Consequently, one may expect that material flow will vary within the SZ.

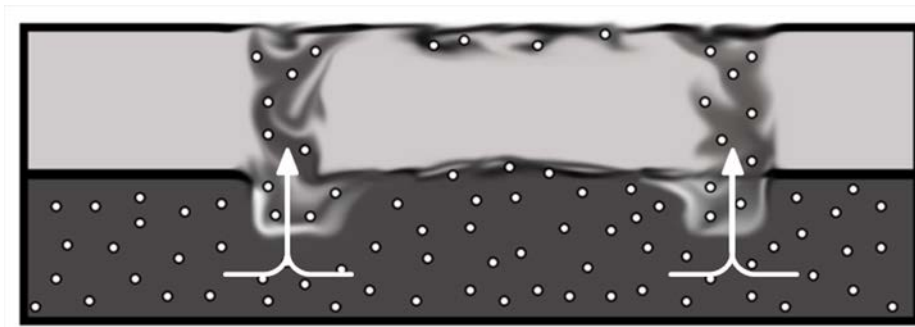


Figure 11: Scheme of material flow (white arrows) and mixing in a friction spot weld; the upper plate represents the PMMA GS and the lower plate the PMMA 6N/2 wt% SiO<sub>2</sub> nanocomposite, with white dots representing silica nanoparticles.

The Raman spectrum of PMMA [30, 31, 32] has previously been described in the literature and will not be discussed here. Because both joined plates consisted of PMMA (PMMA GS and PMMA 6N, respectively), only marginal differences in the spectra were observed.

However, the different PMMA grades could be clearly distinguished. The Raman spectra of PMMA GS and PMMA 6N showed differences in the intensity of their peaks. Thus, polymer mixing could be investigated by selecting suitable signals.

Raman spectroscopic mappings for all three material combinations were carried out in selected areas at the center of the spot welds (Figure 12) and in the lower volume of the SZ (Figure 13). Figure 12a shows an overview of an entire joint, with a red box indicating the measured zone at the center of the joint. Figures 12b, d and f show optical light micrographs of the measured zones. Transmission light microscopy was used because the optical differences of the material could be better detected using transmission rather than reflected light, through which only marginal differences are visible.

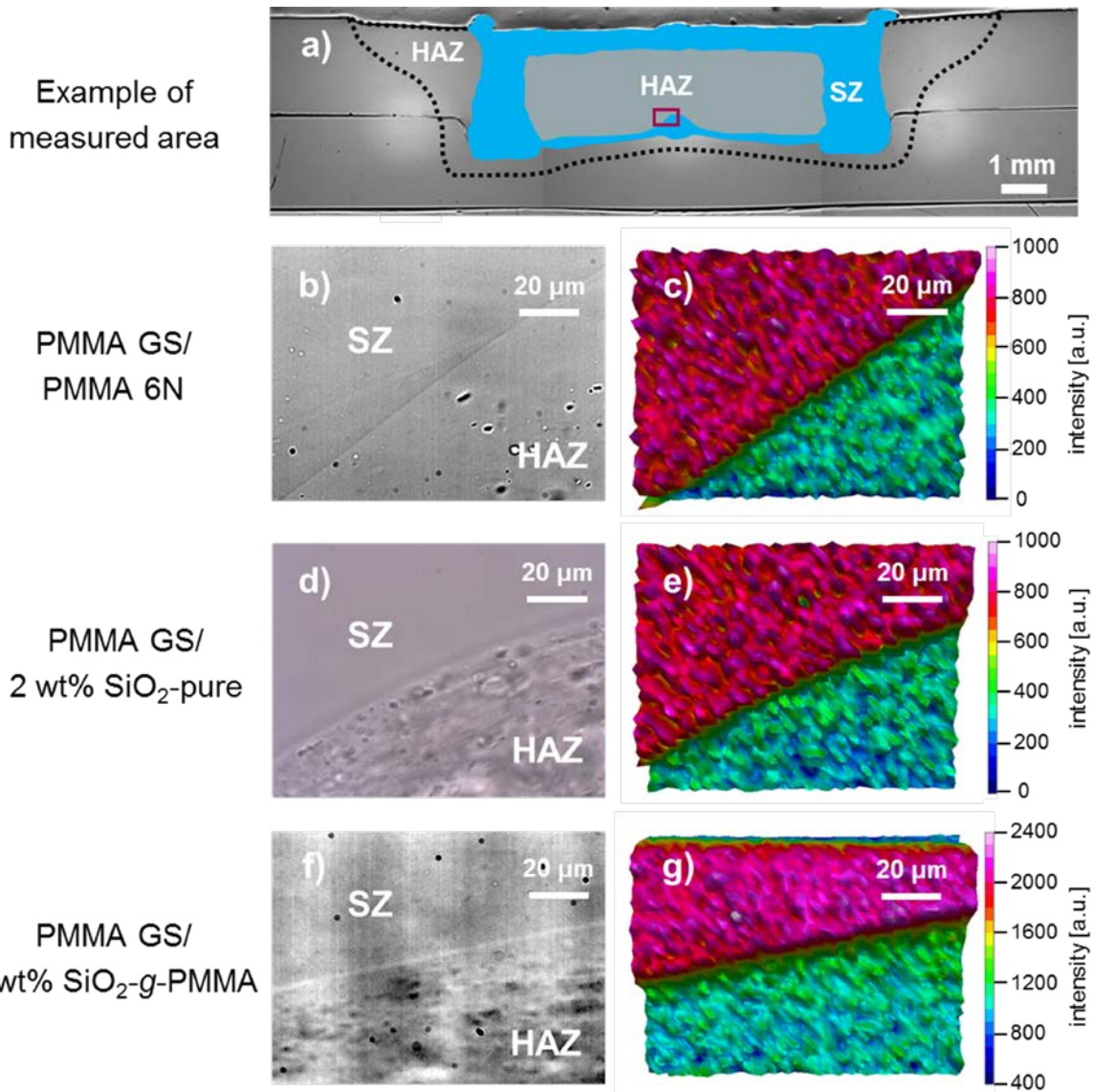


Figure 12: a) Overview of an entire joint; the red box indicates the measured zone at the center of the joint; b), d) and f) optical light microscopy images of the measured zones; c), e) and g) Raman mapping images of the measured zones

Figures 12c, e and g show the results of the Raman mapping of each joint for the peak from  $270\text{ cm}^{-1}$  to  $325\text{ cm}^{-1}$ . A well-defined boundary line between the SZ zone and the outer HAZ can be observed at the center of the PMMA GS/PMMA 6N spot welds (Figure 12b and c). The Raman intensity decreases sharply at this boundary, indicating absent or extremely reduced polymer mixing in this zone. The SZ/outer HAZ interface of PMMA GS/2 wt% SiO<sub>2</sub>-pure (Figure 12e) and that of PMMA GS/2 wt% SiO<sub>2</sub>-g-PMMA (Figure 12f) also show the same behavior with a sharp boundary, as observed in the PMMA GS/PMMA 6N joint. This finding is also supported by the light microscopy results. In this region, no mixing of the polymers could be detected because the pin of the FSpW tool was retracted during the joining process, resulting in a cavity to which the molten polymer could flow. Thus, for all joints,

there was a reduced interdiffusion of molecules over the interface; the interface at this area was probably maintained by secondary forces (e.g., van der Waals) associated with the wetting phenomenon between softened (SZ) and unsoften polymer (HAZ) giving rise to a weld line.

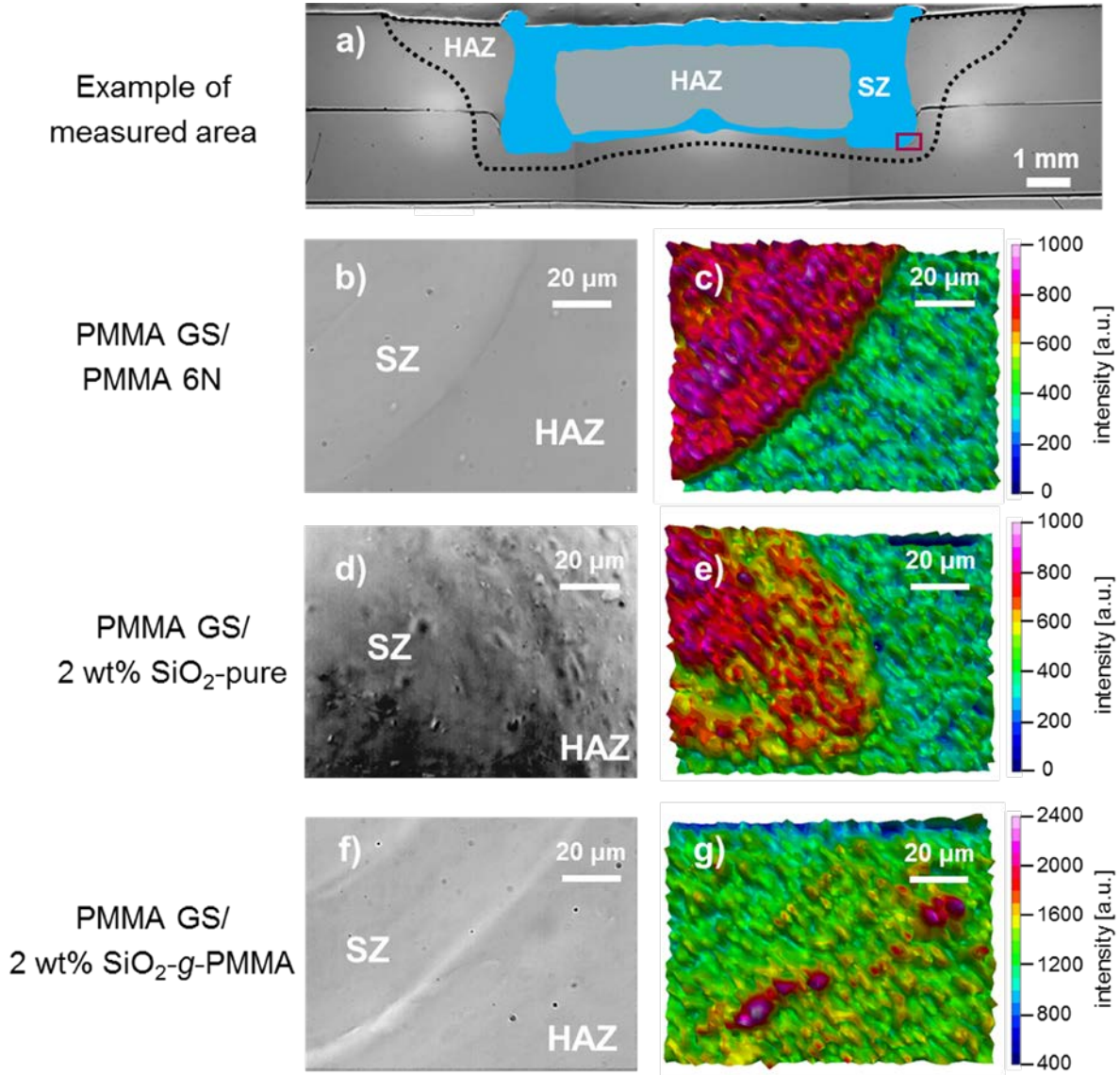


Figure 13: a) Overview of an entire joint; the red box indicates the measured zone at the bottom of the stirring zone; b), d) and f) optical light microscopy images of the measured zones; c), e) and g) Raman mapping images of the measured zones

In addition, Raman mapping was carried out to investigate the material mixing in the lower part of the SZ, where the sleeve was plunged during the joining process. Figure 13a shows an overview of the joint and a schematic representation of the analyzed region (marked with a red box). Figures 13b and c present the transition between the SZ and the outer HAZ of PMMA GS/PMMA 6N. Behavior similar to that exhibited in the examined region at the center of the spot weld can be observed. The PMMA GS and the PMMA 6N can be clearly

differentiated by the sharp drop in the Raman intensity (Figure 13c). The addition of SiO<sub>2</sub>-pure to PMMA 6N led to a better mixing of the polymers, as suggested by the smoother reduction in the Raman intensity at the SZ/outer HAZ interface (Figure 13d and e). This behavior indicates a partial interdiffusion of the polymer chains.

When substituting functionalized SiO<sub>2</sub> nanoparticles for the unfunctionalized SiO<sub>2</sub>, a further improvement in the polymer mixing regime could be observed (Figure 11 f and g). This behavior can be associated with the better randomization of the polymer chains of the PMMA GS and the nanocomposite PMMA (Figure 13b). Optical artifacts observed in the optical microscopy images were located in deeper regions of the sample and were visible because transmitted light was used. From these results, one can conclude that SiO<sub>2</sub> nanoparticles led to better polymer mixing between the two polymer plates in the lower part of the SZ, a region that experienced higher shear rates. The use of functionalized silica nanoparticles appears to have additionally improved polymer mixing during the FSpW process relative to that mixing observed using unfunctionalized nanoparticles. This behavior is probably related to the superior compatibility of the PMMA-coated SiO<sub>2</sub> nanoparticles with the chains of the PMMA GS and the PMMA 6N. Further work is necessary to fully understand the effect of the weld line formation and interdiffusion phenomena of the friction spot welding of PMMA. However, such work is beyond the scope of this study.

### **3.7 Mechanical properties of the FSpW joints**

Single overlap joints were produced using the welding parameters tabulated in caption 2.5 to investigate the shear strength. Figure 14a depicts the obtained lap shear strength and compares it with previously published results of FSp welds of PMMA GS and 2 wt% SiO<sub>2</sub>-pure nanocomposites [26]. In addition, data gathered for other state-of-the-art welding techniques used for PMMA overlap joints are depicted.

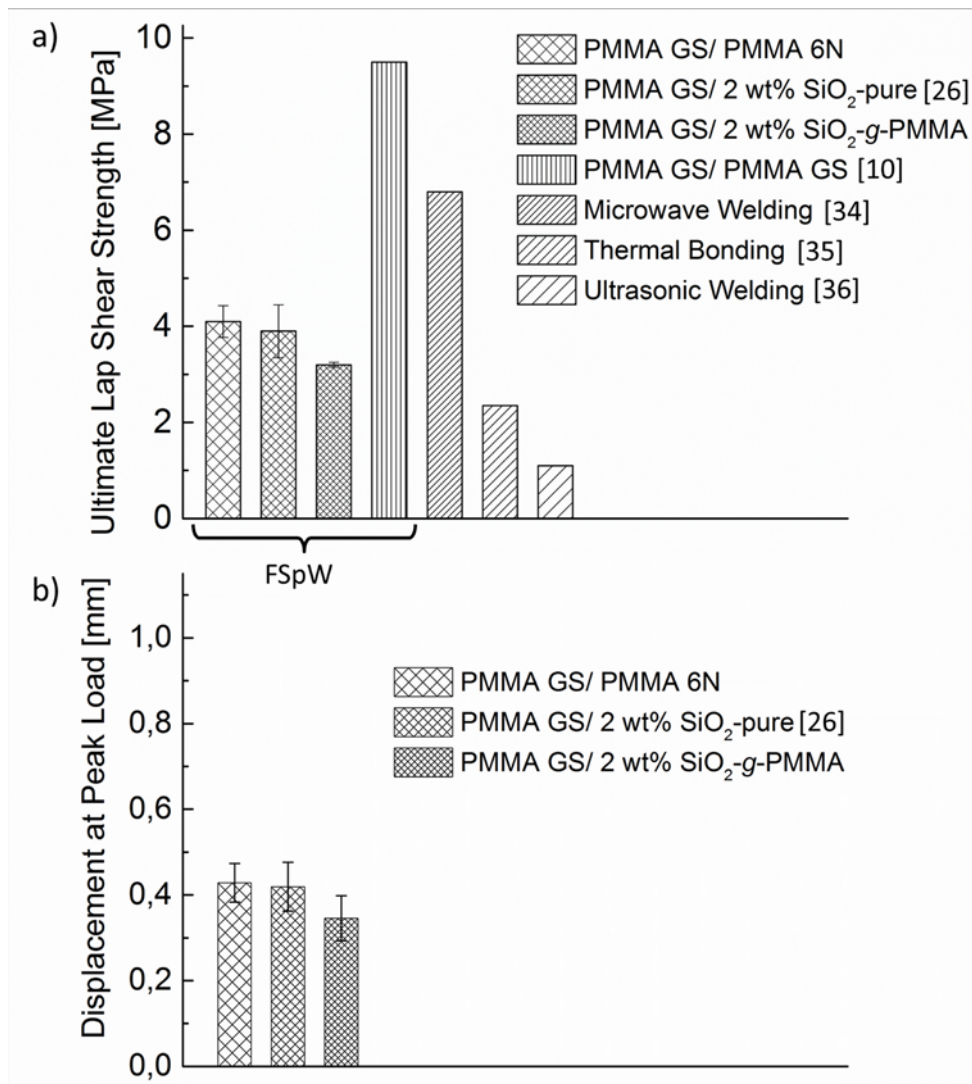


Figure 14: a) Mechanical properties of FSp overlap welds (average of 3 replicates) compared to PMMA welded by other available joining techniques. b) Displacement at peak load of FSp overlap welds on PMMA and PMMA/SiO<sub>2</sub> nanocomposites

An average ultimate lap shear strength of  $4.10 \pm 0.33$  MPa for the reference PMMA GS/PMMA 6N welds was achieved, whereas the PMMA GS/2 wt% SiO<sub>2</sub>-g-PMMA lap joints presented a reduction of approximately 22 % in ultimate lap shear strength, with  $3.20 \pm 0.05$  MPa. Our formerly published results on PMMA GS/SiO<sub>2</sub>-pure single overlap joints [26] showed an average reduction of 7.3 % in ultimate lap shear strength, with a value of  $3.90 \pm 0.50$  MPa. Regarding the displacement at the peak load, a similar trend was observed (Figure 14b). Compared to the reference spot welds of PMMA GS/PMMA 6N ( $0.43 \pm 0.05$  mm) a reduction of approximately 2 % in the displacement at the peak load for PMMA GS/SiO<sub>2</sub>-pure ( $0.42 \pm 0.06$  mm) and a reduction of 21 % for PMMA GS/2% SiO<sub>2</sub>-g-PMMA ( $0.34 \pm 0.05$  mm) welded joints was obtained. These results are in agreement with the observations

and conclusions discussed in Section 3.4 for the tensile testing of the base materials and nanocomposites.

Oliveira et al. [10] reported that FSp welds on PMMA GS 3-mm plates achieved an average lap shear strength of 9.5 MPa. The differences between these results and those reported in the present work can be explained by the larger thickness of the PMMA GS plates. It is well known that due to the geometry of single lap joints, out-of-plane stresses (or so-called secondary bending) occur during lap shear tests [33]. The thicker plates of PMMA GS result in a better stress distribution and reduced out-of-plane stresses in spot welds and thus in higher lap shear strength. In addition, the difference in tensile strength between PMMA GS (approximately 80 MPa) and PMMA 6N (67.2 MPa), approximately 16 %, also contributes increasing out-of-plane stresses, leading to a smaller ultimate lap shear strength of welds with nanocomposites. Compared to microwave welding, which yields a maximum shear strength of 6.8 MPa [34], the FSp welds of PMMA GS with neat PMMA 6N and its SiO<sub>2</sub> nanocomposites showed a smaller shear strength. Compared with the thermal bonding (maximum shear strength of 2.35 MPa) [35] and ultrasonic welding (average shear strength of 1.1 MPa) [36] of PMMA specimens, the results in the present work indicate comparable or higher shear strengths, demonstrating the potential of friction spot welding for joining thermoplastic nanocomposites.

Figure 15 presents the failure modes of lap shear tested specimens on PMMA GS/PMMA 6N, PMMA GS/SiO<sub>2</sub>-pure and PMMA GS/2 wt% SiO<sub>2</sub>-g-PMMA welds. Current theories describing the fracture mechanisms of polymer single lap spot joints welded by frictioning address the existence of four different failure modes during lap shear testing: 1) interface shear failure, through the separation of the plates at the interface, can occur either in weak welds or in brittle polymers [37, 38, 39]; 2) complete or 3) partial plug pull-out of the spot welded area plug [38] (also known as “nugget pull-out” and “partial nugget pull-out” failure modes); and 4) failure of the joining partner, typically observed in strong joints of unreinforced brittle and ductile polymers; fracture usually takes place in one of the base material plates. In this case, a crack nucleates at the interface between the welded area and the base material, ultimately propagating through the thickness of one of the base material plates [37, 38, 39].

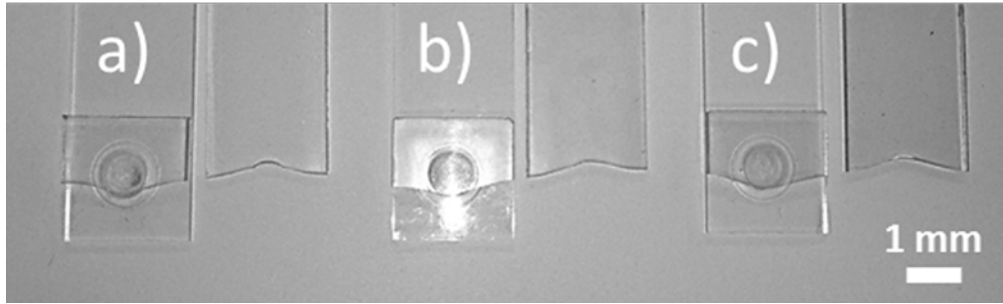


Figure 15: Fractured lap shear specimens of a) PMMA GS/PMMA 6N, b) PMMA GS/SiO<sub>2</sub>-pure and c) PMMA GS/2 wt% SiO<sub>2</sub>-g-PMMA friction spot welded overlap joints.

The tested specimens of PMMA GS/PMMA 6N, PMMA GS/2 wt% SiO<sub>2</sub>-pure and PMMA GS/2 wt% SiO<sub>2</sub>-g-PMMA nanocomposites showed the same failure modes, with the final failure occurring by mode 4 (failure of the joining partner) in the PMMA 6N base material or the SiO<sub>2</sub>-reinforced PMMA 6N nanocomposite, respectively. This failure mode can be explained by the weaker mechanical properties of PMMA 6N and its nanocomposites compared to those of the joining partner PMMA GS. Current knowledge indicates that a crack nucleates at the interface between the welded area and the base material and is deviated to the weaker material, leading to the final failure of the joint. Because one of the base materials collapses, the observation of this failure mode indicates strong spot welds. However, due to the lower tensile strength of the PMMA 6N/2 wt% SiO<sub>2</sub>-g-PMMA nanocomposite compared to that of the neat PMMA 6N and PMMA 6N/2 wt% SiO<sub>2</sub>-pure nanocomposite, lap shear tests also led to a decrease in the ultimate lap shear strength of these joints.

## 4 Conclusions

In this work, the FSpW of a commercial-grade PMMA and a PMMA nanocomposite based on functionalized SiO<sub>2</sub> nanoparticles was performed for the first time. PMMA chains were grafted on SiO<sub>2</sub> nanoparticles via ATRP. The successful grafting of the chains was confirmed by TGA, GPC and ATR-FT-IR investigations. Nanocomposites were produced by a solution casting process, incorporating 2 wt% SiO<sub>2</sub>-pure and 2 wt% SiO<sub>2</sub>-g-PMMA in PMMA 6N. Compared to the PMMA nanocomposite with pristine SiO<sub>2</sub> nanoparticles, the PMMA/2 wt% SiO<sub>2</sub>-g-PMMA showed an improved nanoparticle distribution, as observed by TEM (Figure 5 and 6). Subsequent extrusion led to a further improvement of the nanoparticle distribution. Rheological investigations showed a plateau in the storage modulus  $G'$  at low frequencies (0.01 to 0.03 rad/s) for both SiO<sub>2</sub> nanocomposites, unlike the behavior observed for the neat PMMA 6N (Figure 7). This result indicates that the incorporation of SiO<sub>2</sub> nanoparticles led to elastic particle-particle interactions. Tensile testing showed that the 2 wt% pure SiO<sub>2</sub> nanocomposite and PMMA 6N possessed similar average tensile strengths,  $67.8 \pm 1.9$  MPa and  $67.2 \pm 4.6$  MPa, respectively. The incorporation of 2 wt% SiO<sub>2</sub>-g-PMMA ( $57.7 \pm 6.1$  MPa) led to a decrease of approximately 14 % in the tensile strength. The ductility, as represented by the displacement at the peak load, showed the same trend. Friction spot welded joints of PMMA GS with PMMA 6N, 2 wt% SiO<sub>2</sub>-pure and 2 wt% SiO<sub>2</sub>-g-PMMA nanocomposites were successfully produced. Optical light microscopy images of cross-sections of the joints showed joint microstructures with no defects for all material combinations (Figure 9). In addition, better softening of the polymer in the case of the PMMA GS/2 wt% SiO<sub>2</sub>-pure joint compared to the softening of the polymer in PMMA GS/PMMA 6N joint was detected. Due to the higher heat conductivity of the SiO<sub>2</sub> nanoparticles, the frictional heat generated by the welding tool was conducted more homogeneously through the PMMA plates and thus led to an enhanced softening of the polymer. The functionalization of SiO<sub>2</sub> with PMMA chains led to a further increase in heat dissipation due to the improved nanoparticle distribution. Furthermore, the PMMA chains on the silica nanoparticles appeared to act as a compatibilizer between the two PMMA plates, resulting in a smoother weld line at the spot weld center of the PMMA GS/2 wt% SiO<sub>2</sub>-g-PMMA joint. Raman mappings of the joints were carried out at selected areas at the center of the spot welds and in the lower volume of the stir zone. The different PMMA grades could be detected due to differences in the spectra. Thus, it was observed that no mixing of the polymers occurred in at center of the spot welds for all material combinations (Figure 12). The reference joints on PMMA GS/PMMA 6N showed the same behavior in the lower volume of the SZ (Figure 13).

On the other hand, the functionalization of SiO<sub>2</sub> with PMMA chains led to further improved mixing between the PMMA plates in the lower volume of the SZ (Figure 13).

Lap shear tests of produced overlap welds were carried out for all material combinations. The ultimate weld lap shear strength results reflected the results of the base material tensile strength measurements (the stronger the base material, the stronger the welds produced with the same base material). The PMMA GS/PMMA 6N showed an average shear strength of  $4.10 \pm 0.33$  MPa, whereas the joints of PMMA GS/2 wt% SiO<sub>2</sub>-g-PMMA ( $3.20 \pm 0.05$  MPa) presented a shear strength that was approximately 22 % lower. Previous results of lap shear tests of PMMA GS/2 wt% SiO<sub>2</sub>-pure showed an average shear strength of  $3.90 \pm 0.50$  MPa, and thus a reduction of approximately 7 % compared to the shear strength of PMMA GS/PMMA 6N [26]. Regarding the displacement at the peak load, similar behavior was observed, following the same variation levels observed for the base material (compare graphs from Figure 8 and Figure 14). The displacement at peak load showed a decrease of approximately 2 % for PMMA GS/SiO<sub>2</sub>-pure ( $0.42 \pm 0.06$  mm) and 21 % for PMMA GS/2 wt% SiO<sub>2</sub>-g-PMMA ( $0.34 \pm 0.05$  mm) spot welds compared to the displacement of the reference spot welds of PMMA GS/PMMA 6N ( $0.43 \pm 0.05$  mm).

All produced lap welds failed by mode 4 (failure of the joining partner), the failure mode typically observed in strong spot welds. Final failure occurred at the weakest joining partner, the PMMA 6N base material. Finally a comparison of the current results with those obtained for state-of-the-art techniques was carried out, showing that the spot welds formed in this work were weaker than microwave-welded PMMA joints but stronger than other joints produced by ultrasonic welding and thermal bonding. Therefore, the FSpW of advanced nanocomposite engineering structures, such as headlamps for future cars, appears to be a promising approach, allowing for the production of strong joints within short welding times.

Acknowledgments:

We thank Ivonne Ternes for the functionalization of silica nanoparticles and rheological measurements, Heinrich Böttcher and Dr. Prokopios Georgopoulos for tensile testing and Maren Brinkmann for GPC measurements. In addition, we thank Pedro Oliveira for his support with FSpW. Finally, we would like to acknowledge the financial support of the Landesexzellenzcluster “Integrated Material Systems” and the Helmholtz Association through the Young Investigator Group, “Advanced Polymer Metal Hybrid Structures” (Amancio-Filho, grant no. VH-NG-626).

## References

- [1] Kurauchi T, Okada A, Nomura T, Nishio T, Saegusa S, Deguchi R, Nylon 6-clay hybrid-synthesis, properties and application to automotive timing belt cover, SAE Tech. Pap. 1991; 910584: 1-7.
- [2] Kato M, Kamigaito M, Sawamoto M, Higashimura T, Polymerization of Methyl Methacrylate with the Carbon Tetrachloride/ Dichlorotris-(triphenylphosphine) ruthedum(II)/ Methylaluminum Bis(2,6-di-tert-butylphenoxide) Initiating System: Possibility of Living Radical Polymerization, *Macromolecules* 1995; 28: 1721-1723.
- [3] Wang JS, Matyjaszewski K, Controlled/"Living" Radical Polymerization. Halogen Atom Transfer Radical Polymerization Promoted by a Cu(I)/Cu(II) Redox Process, *Macromolecules* 1995; 28: 7901-7910.
- [4] Haase A, Modifikation technischer Thermoplaste mit polymerfunktionalisierten Silica-Nanopartikeln, PhD Thesis, CAU Kiel (Kiel, Germany), November 2012.
- [5] Chakkalakal GL., Alexandre M, Boschetti-de-Fierro A, Abetz V, Effect of Silica-Coated Poly(butyl methacrylate)-block-poly(methyl methacrylate) Double-Shell Particles on the Mechanical Properties of PMMA Composites. *Macromol. Mater. Eng.* 2012; 297: 887–893.
- [6] Schilling C, dos Santos JF, Method and device for linking at least two adjoining work pieces by friction welding, International Patent Publication 2005; WO/2001/036144.
- [7] Amancio Filho ST, dos Santos JF, Method for joining metal and plastic workpieces, European Patent Specification 2012; EP 2 329 905 B1.
- [8] Esteves JV, Amancio Filho ST, dos Santos JF, Canto LB, Hage Jr. E, Friction Spot Joining of Aluminium 6181-T4 and Carbon Fiber Reinforced Poly(Phenylene Sulfide) in Proc.: ANTEC 2012 PENG, Orlando, FL, USA., April, 2012.
- [9] Amancio-Filho ST, Bueno C, dos Santos JF, Huber N, Hage Jr. E, On the feasibility of friction spot joining in magnesium/fiber-reinforced polymer composite hybrid structures, *Mater. Sci. Eng. A* 2011 ; 528 : 3841–3848.
- [10] Oliveira PHF, Amancio-Filho ST, dos Santos JF, Hage Jr. E, Preliminary study on the feasibility of friction spot welding in PMMA, *Materials Letters* 2010; 64: 2098–2101.
- [11] Plexiglas ® GS Product Description, Germany: Evonik Industries, July 2008.
- [12] Pezow G, Metallographic Etching: Techniques for Metallography, Ceramography, Plastography, ASM International 1999; 2<sup>nd</sup> Edition: 177-179.

- [13] DIN EN ISO 527-1, Plastics – Determination of Tensile Properties– Part 1: General Principles (ISO/DIS 527-1:2010), German version EN ISO 527-1: 2010.
- [14] DIN EN ISO 291, Plastics – Standard Atmospheres for Conditioning and Testing (ISO 291:2008), German Version EN ISO 291: 2008.
- [15] ASTM D3163 – 01, Standard test method for determining strength of adhesively bonded rigid plastic lap-shear joints in shear by tension loading, 2008.
- [16] Oliveira PHF., Amancio Filho ST, dos Santos J F, Hage Jr. E, Influence of the tool material on the microstructure and mechanical properties of PMMA lap joints welded by friction spot, in Proc.: ANTEC 2011 PENG, Boston, MA, USA, May, 2011.
- [17] Kashiwage T, Inaba A, Brown JE, Hatada K., Kitayama T, Masuda E, Effects of Weak Linkages on the Thermal and Oxidative Degradation of Poly(methyl methacrylates), *Macromolecules* 1986; 19: 2160-2168.
- [18] Manring LE, Thermal Degradation of Saturated Poly(methyl methacrylate), *Macromolecules* 1988; 21: 528-530.
- [19] Manring LE, Thermal Degradation of Saturated Poly(methyl methacrylate). 2. Vinyl-Terminated Polymer, *Macromolecules* 1989; 22: 2673-2677.
- [20] Manring LE, Sogah DY, Cohen GM, Thermal Degradation of Saturated Poly(methyl methacrylate). 3. Polymer with Head-to-Head Linkages, *Macromolecules* 1989; 22: 4652-4654.
- [21] Manring LE, Thermal Degradation of Saturated Poly(methyl methacrylate). 4. Random Side-Group Scission, *Macromolecules* 1991; 24: 3304-3309.
- [22] Du B, Handge UA, Majeed S, Abetz V, Localization of functionalized MWCNT in SAN/PPE blends and their influence on rheological properties, *Polymer* 2012; 53: 5491–5501.
- [23] Münstedt H, Triebel C, Temperature dependence of rheological properties of poly(methyl methacrylate) filled with silica nanoparticles, *Polymer* 2011; 52: 1596–1602.
- [24] Münstedt H, Köppl T, Triebel C, Viscous and elastic properties of poly(methyl methacrylate) melts filled with silica nanoparticles, *Polymer* 2010; 51: 185–191.
- [25] Chakkalakal GL, Homopolymer and Block Copolymer Composites Based on Silica Nanoparticles Coated with Polymeric Single or Double Shells Synthesized by Atom Transfer Radical Polymerization, PhD Thesis, CAU Kiel (Kiel, Germany), November, 2011.
- [26] W. S. Junior et al., submitted

- [27] Kochetov R, Andritsch T, Lafont U, Morshuis PHF, Smit JJ, Thermal conductivity of nano-filled epoxy systems, IEEE Conference on Electrical insulation and Dielectric Phenomena 2009; 658-661.
- [28] Lin CB, Wu LC, Friction Welding of Similar and Dissimilar Materials: PMMA and PVC, Polym. Eng. Sci. 2000; 40: 1931-1941.
- [29] Wool RP, O'Connor KM, A theory of crack healing in polymers, J. Appl. Phys. 1981; 52: 5953-5963.
- [30] Thomas KJ, Sheeba M, Nampoorei VPN, Vallabhan CPG., Radhakrishnan P, Raman spectra of polymethyl methacrylate optical fibres excited by a 532 nm diode pumped solid state laser, J. Opt. A: Pure Appl. Opt. 2008; 10: 055303.
- [31] Xingsheng X, Hai M, Qijing Z, Yunsheng Z, Properties of Raman spectra and laser-induced birefringence in polymethyl methacrylate optical fibres, J. Opt. A: Pure Appl. Opt. 2002; 4: 237-242.
- [32] Koenig JL, Angood AC, Semen J, Lando JB, Laser-Excited Raman Studies of the Conformational Transition of Syndiotactic Polymethacrylic Acid in Water, J. Am. Chem. Soc 1969; 91: 7250-7254.
- [33] Ekh J, Multi-Fastener Single-lap Joints in Composite Structures, Royal Institute of Technology SE-100 44 Stockholm, Sweden, 2006.
- [34] Yussuf AA, Sbarski I, Hayes JP, Tran N, Solomon M, Rapid microwave welding of two polymethylmethacrylates substrates, ANTEC 2004:1256-60.
- [35] Sood V, An experimental study on thermal bonding effects of PMMA based microdevices using hot embossing, MSc thesis, University of Texas, Arlington; 2007.
- [36] Souza JM, Study and mechanical evaluation of ultrasonic joints of polycarbonate and poly(methyl methacrylate), MSc thesis, São Paulo: Polytechnic School of University of São Paulo; 2005.
- [37] Bilici MK, Yukler AI, Effects of Welding Parameters on Friction Stir Spot Welding of High Density Polyethylene Sheets, Materials and Design 2012; 33; 545-550.
- [38] Arici A, MERT S, Friction Stir Spot Welding of Polypropylene, Journal of Reinforced Plastics and Composites 2008; 27; 18; 2001-2004.
- [39] Oliveira PHF, Estudo das propriedades e desempenho mecânico de juntas soldadas por fricção pontual de poli (metacrilato de metila) (PMMA), MSc thesis, Universidade Federal de São Carlos, 2012.